Draft version December 18, 2015
Preprint typeset using LaTeX style emulateapj v. 5/2/11

arXiv:1512.05363v1 [astro-ph.GA] 16 Dec 2015

BRIGHT GALAXIES AT HUBBLE'S REDSHIFT DETECTION FRONTIER: PRELIMINARY RESULTS AND DESIGN FROM THE REDSHIFT $z \sim 9-10$ BoRG PURE-PARALLEL *HST* SURVEY

V. Calvi[1], M. Trenti[2], M. Stiavelli[1], P. Oesch[3,4], L. D. Bradley[1], K. B. Schmidt[5,6], D. Coe[1], G. Brammer[1], S. Bernard[2], R. J. Bouwens[7], D. Carrasco[2], C. M. Carollo[8], B. W. Holwerda[7], J. W. MacKenty[1], C. A. Mason[5,9], J. M. Shull[10], and T. Treu[9]

(Dated: December 18, 2015)
Draft version December 18, 2015

ABSTRACT

We present the first results and design from the redshift $z \sim 9-10$ Brightest of the Reionizing Galaxies *Hubble Space Telescope* survey BoRG[z9-10], aimed at searching for intrinsically luminous unlensed galaxies during the first 700 Myr after the Big Bang. BoRG[z9-10] is the continuation of a multi-year pure-parallel near-IR and optical imaging campaign with the Wide Field Camera 3. The ongoing survey uses five filters, optimized for detecting the most distant objects and offering continuous wavelength coverage from $\lambda = 0.35\mu$m to $\lambda = 1.7\mu$m. We analyze the initial ~ 130 arcmin^2 of area over 28 independent lines of sight ($\sim 25\%$ of the total planned) to search for $z > 7$ galaxies using a combination of Lyman break and photometric redshift selections. From an effective comoving volume of $(5-25) \times 10^5$ Mpc^3 for magnitudes brighter than $m_{AB} = 26.5 - 24.0$ in the H_{160}-band respectively, we find five galaxy candidates at $z \sim 8.3 - 10$ detected at high confidence ($S/N > 8$), including a source at $z \sim 8.4$ with $m_{AB} = 24.5$ ($S/N \sim 22$), which, if confirmed, would be the brightest galaxy identified at such early times ($z > 8$). In addition, BoRG[z9-10] data yield four galaxies with $7.3 \lesssim z \lesssim 8$. These new Lyman break galaxies with $m \lesssim 26.5$ are ideal targets for follow-up observations from ground and space based observatories to help investigate the complex interplay between dark matter growth, galaxy assembly, and reionization.

Subject headings: cosmology: observations — galaxies: evolution — galaxies: high-redshift — galaxies: photometry

1. INTRODUCTION

Early galaxies, observed when the Universe was only 500-800 Myr old, need to be identified and studied using deep observations reaching magnitudes $m_{AB} \gtrsim 26$ at near-infrared (near-IR) wavelengths. Essentially, this currently limits the discovery capabilities to observations with the *Hubble Space Telescope* (*HST*). Still, prior to the last servicing mission (2009) *HST* imaging efficiency in the near-IR was not competitive compared to observations in the optical both in terms of detector area and sensitivity. The installation of the Wide Field Camera 3 (WFC3) on-board *HST* has removed this technological barrier. Whereas only a handful of candidates at redshift $z \gtrsim 7$ were known previously (Bouwens et al. 2008, 2010; Bradley et al. 2008; Oesch et al. 2009), the combination of all datasets available to search for high-z galaxies that have been acquired in the last five years now provides a sample approaching 1000 candidates (Bouwens et al. 2012, 2015b; Trenti et al. 2011; Bradley et al. 2012; Oesch et al. 2012, 2014; McLure et al. 2013; Schenker et al. 2013; Finkelstein et al. 2015; Schmidt et al. 2014a; Bradley et al. 2014), reaching up to $z \sim 11$ (400 Myr; Coe et al. 2013). This transformation has been made possible thanks to a combination of ultradeep, small area surveys such as the UDF09 and UDF12[11] campaigns (Illingworth et al. 2013; Ellis et al. 2013), observations targeting cluster-scale gravitational lenses, in particular CLASH[12] (Postman et al. 2012) and the Frontier Fields Initiative (Coe et al. 2015), large area surveys over legacy fields (CANDELS[13]; Grogin et al. 2011; Koekemoer et al. 2011) and with random pointings (BoRG[14]; Trenti et al. 2011).

These observations are allowing a progressively more precise characterization of the evolution of the galaxy luminosity function (LF) in the rest-frame UV ($\lambda \sim 0.15\mu$m). Overall, space-based observations indicate that the UV LF remains well described by a Schechter (1976) form, $\Phi(L) = \Phi^*(L/L^*)^\alpha \exp(-L/L^*)/L^*$, up to $z \sim 8$, similar to what is observed at lower redshift, but with a steepening of the faint-end slope α (e.g., Bouwens et al.

[1] Space Telescope Science Institute, 3700 San Martin Drive, Baltimore, MD 21218, USA. Email: calvi@stsci.edu; valentinacalvi86@gmail.com
[2] School of Physics, University of Melbourne VIC 3010, Australia. Email: michele.trenti@unimelb.edu.au
[3] Yale Center for Astronomy and Astrophysics, Physics Department, New Haven, CT 06520, USA.
[4] Department of Astronomy, Yale University, New Haven, CT 06520, USA.
[5] Department of Physics, University of California, Santa Barbara, CA 93106-9530, USA.
[6] Leibniz-Institut fur Astrophysik Potsdam (AIP), An der Sternwarte 16, 14482 Potsdam, Germany.
[7] Leiden Observatory, Leiden University, NL-2300 RA Leiden, The Netherlands.
[8] Institute of Astronomy, ETH Zurich, CH-8093 Zurich, Switzerland.
[9] Department of Physics and Astronomy, UCLA, Los Angeles, CA, 90095-1547, USA.
[10] CASA, Department of Astrophysical and Planetary Science, University of Colorado, 389-UCB, Boulder, CO 80309, USA.

[11] Hubble Ultra Deep Field 2009, PI. G. Illingworth; Hubble Ultra Deep Field 2012, PI. R. Ellis
[12] Cluster Lensing And Supernova survey with Hubble, PI. M. Postman
[13] Cosmic Assembly Near-Infrared Deep Extragalactic Legacy Survey, PIs: S. M. Faber, H. C. Ferguson
[14] Brightest of Reionizing Galaxies, PI. M. Trenti

2015b). At the bright end, a key open question is whether this trend continues into the core of the reionization epoch ($z \gtrsim 9$), when AGN feedback might be less effective (e.g., Finlator et al. 2011). Observations to answer this question are however difficult because of the rarity of $L > L_*$ galaxies which implies the requirement of large-area surveys. In addition, excess variance because of large-scale structure ("cosmic variance") impacts contiguous surveys (e.g., see Trenti & Stiavelli 2008; Robertson 2010), and gravitational lensing magnification can alter the intrinsic shape, making a Schechter function look closer to a power-law (Wyithe et al. 2011; Barone-Nugent et al. 2015; Mason et al. 2015b; Fialkov & Loeb 2015).

A second motivation for identifying the brightest galaxies during the epoch of reionization is provided by their suitability as targets for follow-up observations, either at infrared wavelengths with Spitzer/IRAC to measure or set limits on galaxy ages and stellar masses (González et al. 2010; Labbé et al. 2015), or with near-IR spectroscopy. The latter has the goals of achieving redshift confirmation via detection of the Lyα emission line, and of investigating how the Lyα equivalent width changes with redshift which can be tied to the evolution of the neutral gas fraction in the intergalactic medium (see Treu et al. 2012). Several groups observed bright $z \gtrsim 7$ galaxies with 8-m class telescopes (Stark et al. 2010; Treu et al. 2012, 2013; Finkelstein et al. 2013; Schenker et al. 2013; Vanzella et al. 2014; Pentericci et al. 2014; Oesch et al. 2015; Roberts-Borsani et al. 2015; Zitrin et al. 2015) reaching the conclusion that detection of Lyα becomes progressively more difficult as the redshift increases. However, the latest observations hint that bright galaxies might have higher equivalent width distributions compared to faint galaxies at $z \gtrsim 7$ (Oesch et al. 2015; Zitrin et al. 2015; Roberts-Borsani et al. 2015). This is a trend that, if confirmed, is the opposite of what happens at $z \lesssim 6$ and might shed light on the topology of reionization and/or on the nature of bright objects at high-z.

With the goals of deriving a cosmic-variance free measurement of the number density of $L > L*$ galaxies at $z \gtrsim 8$ and identifying new targets for follow-up observations, we present here the survey design and preliminary results (first $\sim$ 25% of the area) from a new random-pointing, pure-parallel survey with *HST*/WFC3, optimized for observations at the longest wavelengths accessible to *HST*. The redshift $z \sim 9-10$ Brightest of the Reionizing Galaxies (BoRG[z9-10]) *HST* survey (GO 13767, PI. M. Trenti) is a large program aimed at searching for intrinsically bright ($H_{160}< 27$ mag) and unlensed galaxies during the first 700 Myr in the history of the Universe. BoRG[z9-10] is complementary to the UDF and Frontier Fields datasets, which are primarily identifying galaxies with intrinsic luminosity $L < L_*$. In addition to exploring a new parameter space at $z > 8$, BoRG[z9-10] data also allow us to continue increasing the sample of bright $z \sim 7-8$ galaxy candidates, overall contributing to preparing a sample of excellent targets for follow-up observations during the initial stages of the *James Webb Space Telescope* (*JWST*) mission.

This paper is organized as follows: in Section 2 we describe the design of the BoRG[z9-10] survey, in Section 3 we present our data reduction pipeline, optimized for pure-parallel (undithered) observations, and evaluate the data quality by comparison with dithered data. Section 4 introduces the selection criteria for high-z candidate galaxies from multi-band photometry, with high-confidence candidates at $z > 7$ discussed in Section 5. The resulting constraints on the UV LF at $z \gtrsim 8$ are presented in Section 6, with Section 7 summarizing and concluding our findings. In Appendix A we include a brief discussion of additional dropout candidates that, while satisfying the high-z selection criteria, have a higher chance of being passive galaxies at $z \sim 2$ with colors similar to dropout galaxies at $z \gtrsim 7$.

Throughout this paper we will use the AB magnitude system (Oke & Gunn 1983) and Planck Collaboration et al. (2015) cosmology.

2. DESIGN OF THE SURVEY

The *HST* WFC3 BoRG[z9-10] survey is a large (480 orbits) pure-parallel imaging program with the nominal goal of imaging ~ 550 arcmin^2 over 120 independent lines of sight using the near-IR filters of the Frontier Fields and HUDF12 programs: F105W (Y_{105}), F125W (J_{125}), F140W (JH_{140}), and F160W (H_{160}), complemented by F350LP, a long-pass red optical filter, achieving medium depth sensitivity ($m_{AB} \sim 26.5-27.5$; 5σ point source). The main science driver of BoRG[z9-10] is the identification of galaxy candidates at $z > 8$ from broadband colors, with a survey design optimized to constrain the bright end of the LF at $z \sim 9-10$ when the Universe was ~ 500 Myr old. For this design, the filter set provides continuous wavelength coverage from $\sim 0.35\mu$m to $\sim 1.7\mu$m (Figure 1). High-z objects are selected using a combination of the Lyman break (dropout) technique (Steidel et al. 1996) and the Bayesian photometric redshift estimates (BPZ; Benítez 2000), as discussed in Section 4.

BoRG[z9-10] is a pure-parallel program; the WFC3 observations are carried out while *Hubble* is pointed at a primary target using the Space Telescope Imaging Spectrograph (STIS) or Cosmic Origin Spectrograph (COS), both ~ 6 arcmin away from WFC3 in *HST* focal plane. In addition, since primary spectroscopic targets are typically in the local Universe and/or at low redshift ($z \lesssim 3$), the volume imaged at $z \gtrsim 6$ by WFC3 pure-parallel observations is uncorrelated with the primary targets. WFC3 pointings in BoRG[z9-10] have variable exposure times, from $\sim$ 7000s (3 orbits) to $\sim$ 19000s (8 orbits), with the specific duration of each opportunity determined by the primary program.

The non-contiguous nature of a large-area survey like BoRG[z9-10] is ideal for determining an unbiased measurement of the number density of galaxies at high redshift, since these objects are strongly clustered (Barone-Nugent et al. 2014). In contrast, the number counts from a contiguous large area survey are significantly affected by sample ("cosmic") variance, which typically introduces an additional systematic uncertainty that is of the order of (and potentially exceeds) the Poisson noise (Trenti & Stiavelli 2008).

The advantage of observing a large number of independent lines of sight balances some of the challenges of pure-parallel observations. Specifically, the depth and image quality are non uniform across the pointings. In addition to different exposure times, the foregrounds also vary (e.g. Galactic dust extinction). Furthermore, pure-parallel observations are not dithered because this would

conflict with the pointing of the primary opportunity. To minimize the impact of these limitations, we developed a highly optimized observation design (phase II) of BoRG[z9-10]. Specifically:

- We prioritized the use of primary observations that had the longest observing time available for parallel imaging and the least amount of Galactic extinction (estimated using the Schlafly & Finkbeiner 2011 maps), although our degrees of freedom were limited because the pool of available opportunities (577 orbits) was only marginally larger than the program allocation (480 orbits).

- To ensure high image quality (i.e to minimize spurious sources) and robust identification/rejection of cosmic rays, we adopted frequent readings (every 100s) of the near-IR detector (SPARS100 mode), so as to have the detector well sampled. For each filter we also scheduled independent exposures in at least two different orbits. The latter choice allows us to take advantage of any dithering induced by small changes in the roll angle of *HST* between subsequent orbits. Observations in F350LP (optical CCD detector) consist of at least three independent exposures, each with integration time[15] 400s$\leq t_{exp} \leq$800s, although these might be scheduled in a single orbit in order to minimize the use of the WFC3 channel select mechanism[16].

- We set a reference relative depth between the filters, and then divided the total exposure time available in each opportunity accordingly. Our goal is to achieve, after correcting for Galactic dust extinction, a near-uniform depth in the near-IR filters, while F350LP observations reach 0.5 mag deeper. Specific opportunities may deviate from the target depths because of the need to satisfy the requirements discussed above on image quality and/or because of readout conflicts with the primary observations. A summary of the exposure times for each pointing analyzed in this paper is presented in Table 1.

- F105W observations are scheduled in the central part of the orbit to minimize the impact of elevated background noise induced by Earth-glow (Brammer et al. 2014). In addition, F160W images are taken last in each orbit, so as to be least impacted by any detector persistence from previous observations. This approach guarantees that any ghost source induced by persistence is brighter in the dropout filter compared to the detection filter, making it impossible to select it as a dropout candidate. This design choice has been used in our pure-parallel observations since Cycle 17 (Trenti et al. 2011) and has demonstrated effectiveness in preventing the introduction of spurious dropout sources due to persistence.

[15] The interval lower boundary is set to ensure sufficient background so that Charge-Transfer Efficiency (CTE) effects are not impacting the readout, while the upper boundary limits the number of cosmic rays present in each exposure.

[16] The channel select mechanism is a potential non-redundant point of failure for the instrument. Therefore we designed the observations to use it no more than one time after the start of each opportunity.

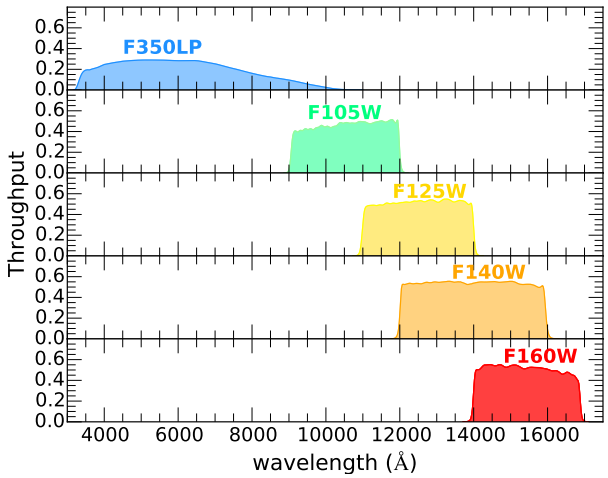

Figure 1. Transmission curves of our filter set, from visible to IR: F350LP, F105W (Y_{105}), F125W (J_{125}), F140W (JH_{140}), and F160W (H_{160}) as labeled. We used two complementary, non overlapping sets of IR filters, namely Y_{105}-JH_{140} and J_{125}-H_{160}, for an optimal identification of high-z galaxies through the dropout technique (Stanway et al. 2008).

The BoRG[z9-10] design is inspired by its predecessor BoRG[z8] (Trenti et al. 2011), which was optimized for detection of galaxies at $z \sim 8$ and covered about 350 arcmin^2 of area over 71 independent pointings by its completion (Schmidt et al. 2014a). With respect to the past survey there are two main differences: (1) the use of four IR filters, with the addition of F140W, crucial to identify $z \sim 9-10$ galaxies, and the substitution of F098M in favor of F105W. The latter choice is motivated by the goal of having a contiguous non-overlapping pair of filters F105W/F140W which is optimal for selection of $z \sim 9$ galaxies (Stanway et al. 2008); (2) changing F606W to F350LP to collect more efficiently all photons at wavelengths shorter than the CCD detector cutoff ($\sim 1\mu$m; see Figure 1). As discussed in Section 4, these choices are optimal for constructing clean samples of $z > 8$ galaxies, but they imply an increased contamination from low-z interlopers for the $z \sim 7-8$ sample (Section 6.2).

Finally, BoRG[z9-10] represents a collection of medium-deep near IR and optical imaging with a legacy value beyond the identification of rare galaxies during the epoch of reionization. The high number of independent lines of sight, distributed over a wide range of Galactic longitudes and latitudes, has enabled the study of Galactic structure by identifying faint M, L, and T dwarf stars (Ryan et al. 2011; Holwerda et al. 2014).

3. DATA REDUCTION

In this work we consider all the BoRG[z9-10] observations acquired until June 14, 2015, providing 42 pure-parallel opportunities. Six pairs of opportunities cover partially overlapping regions of the sky, which we combined to maximize the depth of the observations over the common area, reaching up to $t_{exp} = 18700$s in the deepest case. Of these 36 independent pointings, we discarded 8 fields from the analysis because of guide star acquisition

failure[17], or because of excessive stellar crowding (in case primary observations had local Universe targets). Thus in the remainder of the paper we focus on 28 independent lines of sight suitable for searching high-z galaxies, giving a total area of ~ 130 arcmin^2. Details of each field are provided in Table 1.

Data were downloaded from the MAST archive[18], and individual exposures processed through the standard `calwf3` pipeline to apply bias correction (UVIS only), dark subtraction, and flat-fielding using the most up-to-date reference files.

In addition to running `calwf3`, processing of F350LP included a correction for the Charge-Transfer Efficiency effect (CTE[19]; Noeske et al. 2012; Anderson 2014). For all filters, we performed a customized extra step to remove residual cosmic rays and/or detector artifacts such as unflagged hot pixels by using a Laplacian edge filtering algorithm developed by van Dokkum (2001) and previously used for BoRG[$z8$] observations (Bradley et al. 2012; Schmidt et al. 2014a).

Despite the optimization of the orbit and filter sequence, a small number of F105W exposures suffered from time-variable backgrounds during the exposure (Brammer et al. 2014). These backgrounds, caused by airglow emission in the upper atmosphere, can compromise the default up-the-ramp processing of the `calwf3` pipeline and corrupt the noise properties of the resulting calibrated images (see also Koekemoer et al. 2013)[20]. In these cases we remove the variable component of the background as sampled at multiple times within the exposure and reprocess the background-flattened sequences with `calwf3` (Brammer et al., in preparation[21]).

To obtain the final science images in each filter we used the `Drizzlepac` software (Gonzaga 2012), aligning all exposures to a common frame and using `AstroDrizzle` to construct final science images and inverse variance maps (wht image) with a scale of $0\farcs08$ pixel^{-1}. Since the drizzling process introduces correlated noise regardless of the kernel used (Casertano et al. 2000; Oesch et al. 2007), we derived a rescaling factor for the inverse variance maps, following the procedure described by Trenti et al. (2011). In short, we construct a preliminary source catalog using `SExtractor` (Bertin & Arnouts 1996), and then place empty apertures ($0\farcs32$ radius) over sky regions performing aperture photometry with the same code. The errors provided by `SExtractor` depend on the variance map, defined from the inverse variance weight map as:

$$\frac{1}{\sqrt{\text{wht image}}} \tag{1}$$

The rms map can be rescaled by a constant factor to ensure that the median error quoted for the photometry in an empty aperture is equal to the variance of the sky flux measurements. The typical rescaling factors we applied are 1.06 for the IR filters, and 1.33 for F350LP images. In addition to normalizing the variance maps, the noise measurements done as part of this procedure allow us to quantify the limiting magnitude of each image. The limiting magnitudes for individual fields and filters are reported in Table 1.

3.1. *Pure-parallel image quality*

As discussed in Section 2, pure-parallel imaging is not dithered, potentially affecting the data quality of the photometry. Thanks to a follow-up program of a Y-dropout overdensity in BoRG[$z8$] (see Trenti et al. 2012), we have both pure-parallel and dithered observations of overlapping area in the same IR filters. Previously, we combined all available data to maximize the depth of the observations, arriving at identifying the brightest dropouts of the region at very high S/N (object borg_1437+5043_1137 with $J_{125}= 25.76 \pm 0.07$ mag detected at $S/N_{125} \sim 20$; Schmidt et al. 2014a). Here, we re-processed the original pure-parallel observations in F125W ($t_{exp} = 2500$ s) with our latest pipeline, and separately we analyzed the dithered (primary GO) follow-up observations, combining a total of $t_{exp} = 2300$ s of data and using a pixel scale of $0\farcs08$ pixel^{-1} with the goal of obtaining the closest analog possible to the pure-parallel image. Visual inspection of the two science images, which are shown in the top panels of Figure 2, immediately highlights the near-equivalence of the pure-parallel data to the dithered ones. To quantify the photometric accuracy, we selected 400 empty sky regions in each image and performed aperture photometry (radius $r = 0\farcs32$) obtaining the noise distribution shown in the bottom panel of Figure 2. The variance σ of the distribution for the pure-parallel and dithered dataset are 0.10 and 0.11, respectively, corresponding to $m_{lim} = 28.7$ (pure-parallel) and $m_{lim} = 28.6$ (dithered) in the J_{125}-band, in agreement with the exposure time calculator estimate of a $\Delta m_{lim} = 0.06$ due to the slight difference in exposure time. Furthermore, within statistical uncertainty, the two distributions are equivalent (Kolmogorov-Smirnov statistics p-value 99%). These tests demonstrate that the lack of dithering has essentially no impact on the photometry from pure-parallel data, which we can consider equivalent to that of dithered data with the same exposure time within our analysis uncertainty of $\Delta m \lesssim 0.1$.

3.2. *Source catalog construction*

To construct source catalogs we ran `SExtractor` in dual-image mode. For each field, we combined all the frames taken in F140W and F160W with `AstroDrizzle` to create a detection image and a combined weight map, which has been normalized for correlated noise (see Section 3). As a necessary condition for inclusion in the catalog, we required objects to have at least nine contiguous pixels with signal-to-noise ratio per pixel $S/N \geq 0.7$. Subsequently, we post-process the catalog to retain only sources with isophotal $S/N \geq 8$ in the detection image.

Photometry was performed in each filter via `SExtractor` dual-mode using the detection image to define source positions and isophotal contours. As in BoRG[$z8$], we adopt MAG_AUTO as the total magnitude of each source, while the signal to noise S/N is defined as:

$$\frac{S}{N} = \frac{\text{FLUX_ISO}}{\text{FLUXERR_ISO}}$$

[17] In this case the observations might be repeated in the future depending on the request by the primary observer.

[18] http://archive.stsci.edu/hst/search.php

[19] STScI CTE tools are available at http://www.stsci.edu/hst/wfc3/tools/cte_tools

[20] Note that this source of noise is not related to the pure-parallel nature of the observations.

[21] https://github.com/gbrammer/wfc3/blob/master/reprocess_wfc3.py

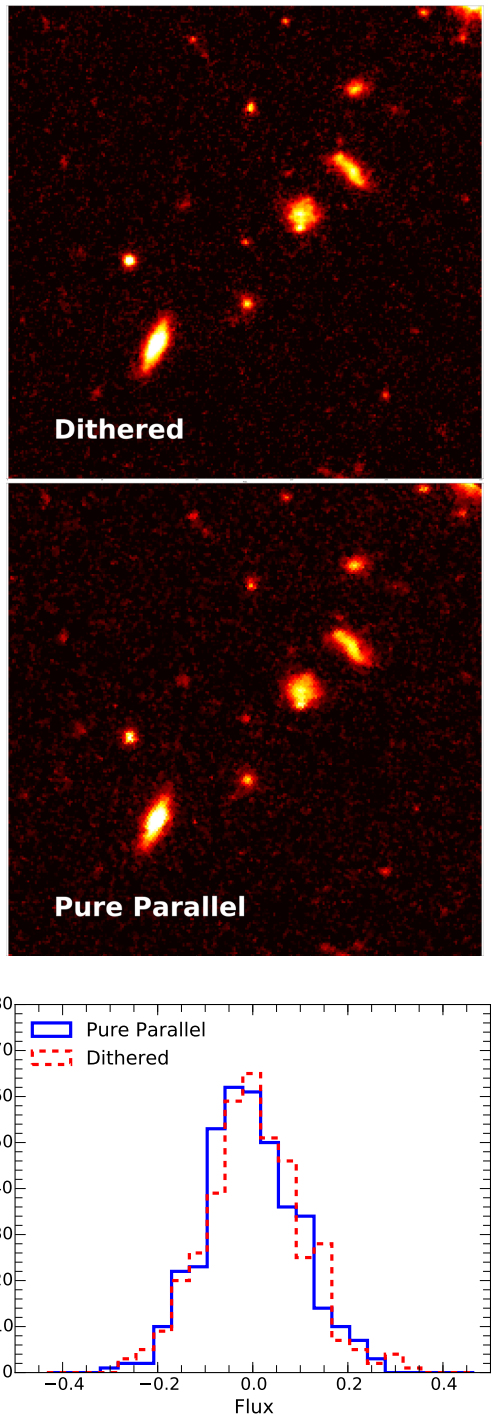

Figure 2. Top panel: F125W data comparison between pure-parallel (bottom figure, exposure time 2500s, GO 11700) vs. dithered (top figure, exposure time 2300s, GO 12905) dataset for the BoRG[$z8$] field borg_1437+5043 (Trenti et al. 2011, 2012; Bradley et al. 2012; Schmidt et al. 2014a). The cutout images have a $20''.0$ side and are centered on the bright $z \sim 8$ galaxy borg_1437+5043_1137 (J_{125}=26 mag). Bottom panel: The histograms show the noise distribution in 400 empty apertures (sky-subtracted) with $r = 0''.32$, which quantitatively demonstrates the near-equivalent data quality of pure-parallel (solid blue line) and dithered datasets (dashed red line).

(see Stiavelli 2009). Finally, colors are calculated from `SExtractor` isophotal magnitudes (MAG_ISO), without applying PSF matching, following the established practice for the BoRG survey (see Trenti et al. 2012). To account for Galactic extinction in each field, the official magnitude zeropoints[22] ($\mathrm{Zpt}_{F350LP} = 26.9435$ mag, $\mathrm{Zpt}_{F105W} = 26.2687$ mag, $\mathrm{Zpt}_{F125W} = 26.2303$ mag, $\mathrm{Zpt}_{F140W} = 26.4524$ mag, $\mathrm{Zpt}_{F160W} = 25.9463$ mag) have been corrected using the maps by Schlafly & Finkbeiner (2011)[23].

To be included in the catalogs, objects need to have segmentation maps that are associated to pixels with non-zero weight maps in all five filters of the survey. For example, we excluded sources that fall on the gap between the two CCD detectors and thus lack photometry in F350LP.

Finally, we used external persistence maps[24], which are released shortly after the observations, to flag any source in the catalog that appears to be either spurious or affected by persistent charge. Specifically, for each image and for each filter, we created a mask that includes all pixels in the released map with persistence value above $0.01\mathrm{e}^-/\mathrm{s}$, and flagged all sources in the catalog that include at least one persistent pixel.

3.3. *Bayesian Photometric Redshifts*

For an optimal use of the full photometric information from our five bands survey, we ran the BPZ code by Benítez (2000) (see also Coe et al. 2006) on all detected sources. We use spectral energy distribution (SED) model templates as described in Benitez et al. (2014) (but see also Rafelski et al. 2015). Originally based on PEGASE models including emission lines (Fioc & Rocca-Volmerange 1997), these SEDs are recalibrated to match the observed photometry of galaxies with spectroscopic redshifts from FIREWORKS (Wuyts et al. 2008). They include five early types, two late types, and four starbursts. BPZ allows for interpolation between adjacent templates. These 11 templates were selected to encompass the ranges of metallicities, extinctions, and star formation histories derived from galaxy observations at low and high redshift. Because of the degeneracy between redshift and intrinsic galaxy properties such as age, dust content, and presence of emission lines, photometric redshift estimates for classes of rare objects with properties similar to galaxies at $z > 6$ are affected by uncertainties that are difficult to quantify. Therefore, rather than relying only on photo-z to identify high-z objects, we opt primarily for a Lyman break selection, as discussed below. Given the challenges and uncertainty associated to the definition of an informed prior on the relative likelihood of solutions that have dropout-like colors but are lower-redshift interlopers, we make the minimal assumption of adopting a flat prior on the redshift distribution.

4. SELECTION OF HIGH-REDSHIFT GALAXIES

From the source catalogs, we identify high-z objects using the Lyman break technique (Steidel et al. 1996, 1999), with a set of selection criteria similar to the ones used in legacy fields (e.g., see Bouwens et al. 2015b) but

[22] http://www.stsci.edu/hst/wfc3/phot_zp_lbn
[23] http://irsa.ipac.caltech.edu/applications/DUST
[24] http://archive.stsci.edu/prepds/persist/search.php

adapted to the specific filter set of BoRG[z9-10]. Our general requirements are a clear detection of the source at long wavelengths, the presence of a strong break in a pair of adjacent, non-overlapping filters (which minimizes contamination; see Stanway et al. 2008), a conservative non-detection in blue bands to reject interlopers effectively ($S/N < 1.5$)[25], and a relatively flat spectrum redward of the break, again imposed to control for contamination. In addition to $S/N \geq 8$ in the *detection image* imposed when constructing source catalogs, these requirements translate into:

- For $z \sim 9$ sources (Y_{105}-JH_{140} dropouts)

$$S/N_{350} < 1.5$$
$$S/N_{140} \geq 6$$
$$S/N_{160} \geq 4$$
$$Y_{105} - JH_{140} > 1.5$$
$$Y_{105} - JH_{140} > 5.33 \cdot (JH_{140} - H_{160}) + 0.7$$
$$JH_{140} - H_{160} < 0.3$$

  These selection criteria used to identify Y_{105}-JH_{140} dropouts determine a selection function peaked at $z = 8.7$ and with a 95% confidence region spanning from $z = 7.7$ up to $z = 9.7$ (see Figure 3).

- For $z \sim 10$ sources (J_{125}-H_{160} dropouts)

$$S/N_{350} < 1.5$$
$$S/N_{105} < 1.5$$
$$S/N_{160} \geq 6$$
$$J_{125} - H_{160} > 1.3$$

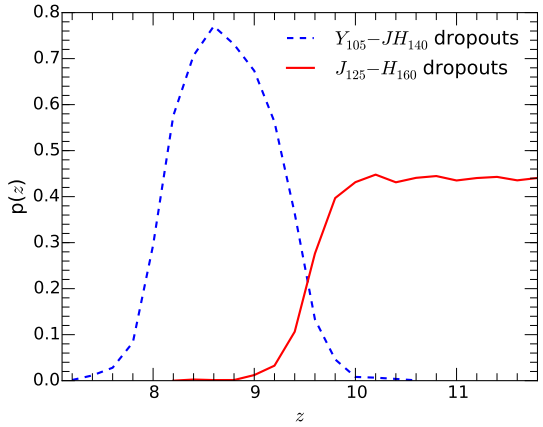

Figure 3. Distribution of the probability p(z) associated to the selection function as derived from our simulations (see Section 6.1) for the field borg_0116+1425 representative of a typical BoRG[z9-10] pointing.

[25] For a Gaussian distribution of noise, imposing a blue non-detection at $S/N < 1.5$ in a single filter implies that we can have up to $\sim 93\%$ completeness of the high-z sample, or up to $\sim 87\%$ completeness if the non-detection is required in two filters.

Finally, we construct a sample of $z \sim 7-8$ galaxy candidates selected on the basis of a drop in Y_{105}-J_{125}, widely used in the UDF and CANDELS surveys, but potentially more prone to contamination in absence of extensive multi-filter optical data because of the partial overlap between F105W and F125W (see Stanway et al. 2008 for a discussion of how contamination is increased by overlapping filters):

$$S/N_{350} < 1.5$$
$$S/N_{125} \geq 6$$
$$S/N_{140} \geq 6$$
$$S/N_{160} \geq 4$$
$$Y_{105} - J_{125} > 0.45$$
$$Y_{105} - J_{125} > 1.5 \cdot (J_{125} - H_{160}) + 0.45$$
$$J_{125} - H_{160} < 0.5$$

In order to avoid duplication, if a candidate satisfies more than one selection criterion, it is assigned to the highest redshift sample.

We further refine the dropout samples by imposing a cut on the `SExtractor` stellarity measurement, which indicates the likelihood of having a point source, and we require CLASS_STAR< 0.95. Note that this cut was not introduced primarily to reject stellar contamination, but rather to automatically and objectively remove spurious detections induced by hot/warm pixels that may have survived both the standard STScI calibration and our Laplacian filtering.

As an additional step to remove false detections from the dropouts catalogs, VC, MT, and LB independently inspected candidates visually, using final drizzled (and individual flt files when needed), to reject all, and only those, sources associated to detector artifacts, hot pixels and diffraction spikes.

Finally, to control contamination from low-z interlopers in the Lyman break samples, we ran the Bayesian photometric code BPZ (Benítez 2000; see Section 3.3 for details) and retained in the final candidate sample only objects with photo-z peaked at $z > 7$.

4.1. *Alternative Catalogs for $z > 7$ sources*

For the purposes of deriving LFs, we consider as optimal our choice to construct catalogs starting from the Lyman break selection, since it allows us to calculate the source recovery efficiency as a function of input magnitude and redshift, which is then used to constrain the number density of high-z sources.

However, the Lyman Break Galaxy (LBG) selection is based on a binary decision outcome regarding inclusion of candidates in the high-z source catalog, neglecting the impact of photometric uncertainties that scatter objects in and/or out of the selection region (Su et al. 2011). Therefore, to investigate whether we are missing objects, we employed an alternative selection by searching for sources in our photometric catalogs that have high-z solutions. Following McLure et al. (2013), we required non-detection in the optical ($S/N_{350} < 2$) as a necessary condition, and impose stellarity CLASS_STAR< 0.95, as well. Then, we selected sources that have the peak of the redshift probability distribution function at $z > 7$.

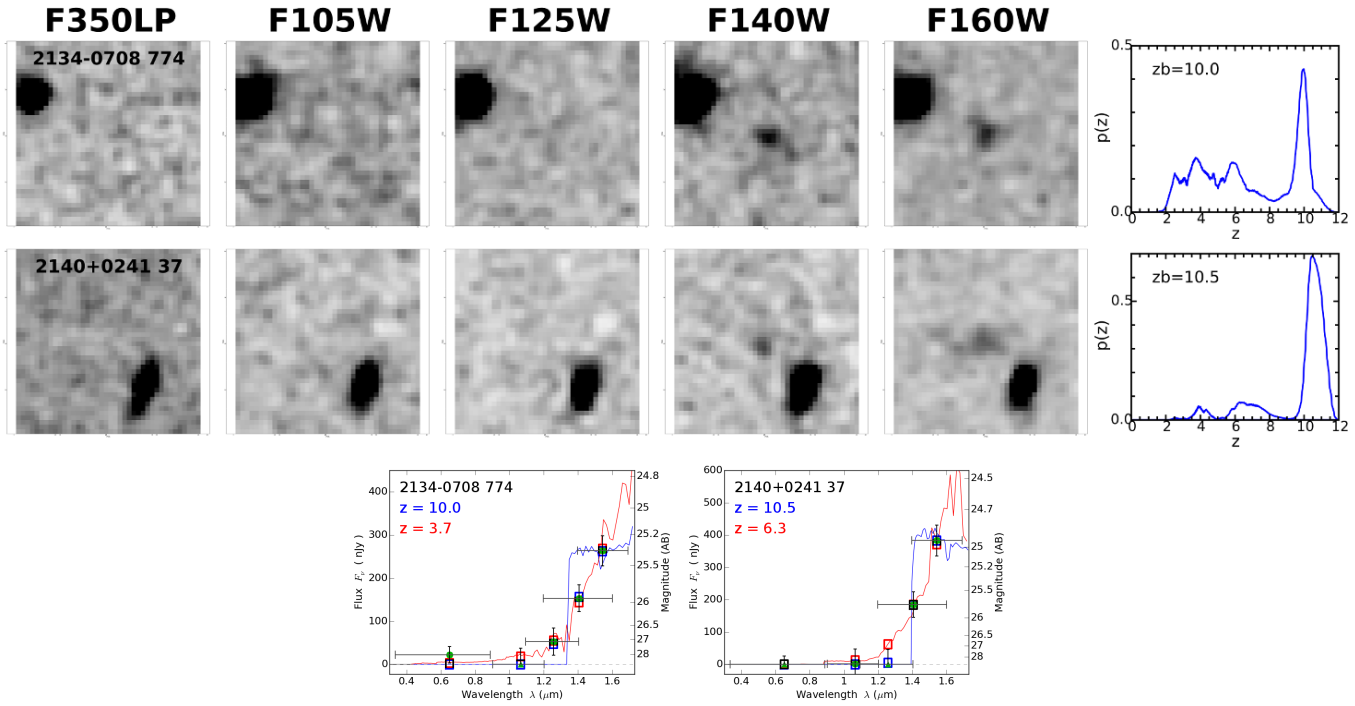

Figure 4. Postage-stamp images of the J_{125}-H_{160} dropout candidates listed in Table 2. The cutout images are $3\farcs2 \times 3\farcs2$, each one centered on the candidate dropout galaxy. Right panels show the photometric redshift probability distribution p(z) obtained by running BPZ using a flat prior. Bottom panels show the spectral energy distribution for both the the low (red) and high-z (blue) solutions. Right axes in the SED plots show the total magnitudes from SExtractor MAG_AUTO.

In addition, we evaluated the sensitivity of the source selection to the construction of catalogs with a combination of F140W and F160W. For this, we produced alternative catalogs using only F160W as detection image. The results of this selection are summarized in Appendix A.

5. RESULTS: HIGH-z CANDIDATES

Our sample of high confidence, high-z candidates consists of five bright sources detected at $S/N > 8$ with inferred redshift peaking at $z > 8$. Two are J_{125}-H_{160} dropouts ($z \sim 10$) and three are identified as Y_{105}-JH_{140} dropouts, with their most probable redshift estimated at $z > 8.3$. Table 2 contains the photometry for these sources, Figures 4 and 5 show cutout images centered on each galaxy, the p(z) distribution, and the best low and high-z spectral energy distributions (SEDs) fitting the photometry of the candidates. Finally, the sample reported in this paper is augmented by four Y_{105}-J_{125} dropouts, with redshift $z \sim 7.3-8$ (see Table 3 and Figure 6). The IR color-color selection regions are shown in Figures 7 and 8.

Our alternative search for high-z candidates from the Bayesian photometric redshifts (Section 4.1) does not identify additional $z > 7$ sources. This provides confidence that our catalog of bright sources detected at high S/N is not missing robust candidates, irrespective of the selection technique used.

5.1. $z \sim 10$ *galaxies* (J_{125}-H_{160} *dropouts*)

The selection of the highest redshift galaxies in BoRG[z9-10] relies primarily on one color (J_{125}-H_{160}; see Figure 8), associated to non detection in the bluer bands (F350LP and F105W). F140W is used to verify whether the object is detected in a second, independent band, and to refine the photometric redshift estimates. Figure 3 shows the expected redshift distribution of the dropouts for a flat input distribution in one representative field, obtained through artificial source recovery simulations (Oesch et al. 2007, 2009, 2012 and Section 6.1). The figure clearly indicates that the color criteria adopted select sources at $z \gtrsim 9.5$. Our sample consists of two of them:

borg_2134-0708_774 is a galaxy with magnitude H_{160}=25.35 and a very red J_{125}-H_{160} color (J_{125}-H_{160}= 1.74). The photometric redshift probability distribution peaks at $z = 10.0$, implying $M_{AB} \sim -22.2$, albeit there is a broad wing of lower z solutions. The source is clearly resolved and shows extended structure in both the JH_{140} and H_{160}-band images. Its intrinsic half-light radius is $r_e = 0\farcs23$, after correction for the broadening introduced by the Point Spread Function (PSF). Interestingly, the dropout is in close proximity ($1\farcs46$ center to center) to a foreground galaxy of magnitude H_{160}=23.22. The photometric redshift distribution for the foreground is very broad, but given its compact size, it is likely at $z \gtrsim 0.5$ and thus can provide at least some gravitational lensing magnification. We estimated the possible range of magnification using the modeling framework developed by Barone-Nugent et al. (2015) and Mason et al. (2015b). Both methods suggest that the magnification is modest ($\mu \lesssim 1.5$) assuming a typical mass-to-light ratio, because the foreground galaxy is relatively faint. The maximum $\mu \sim 1.5$ is expected if the foreground galaxy is at $z \sim 2$, while we predict $\mu = 1.2 \pm 0.1$ in case of a deflector at $z \sim 0.8$, which is the redshift at which the lensing optical depth peaks (see Mason et al. 2015b).

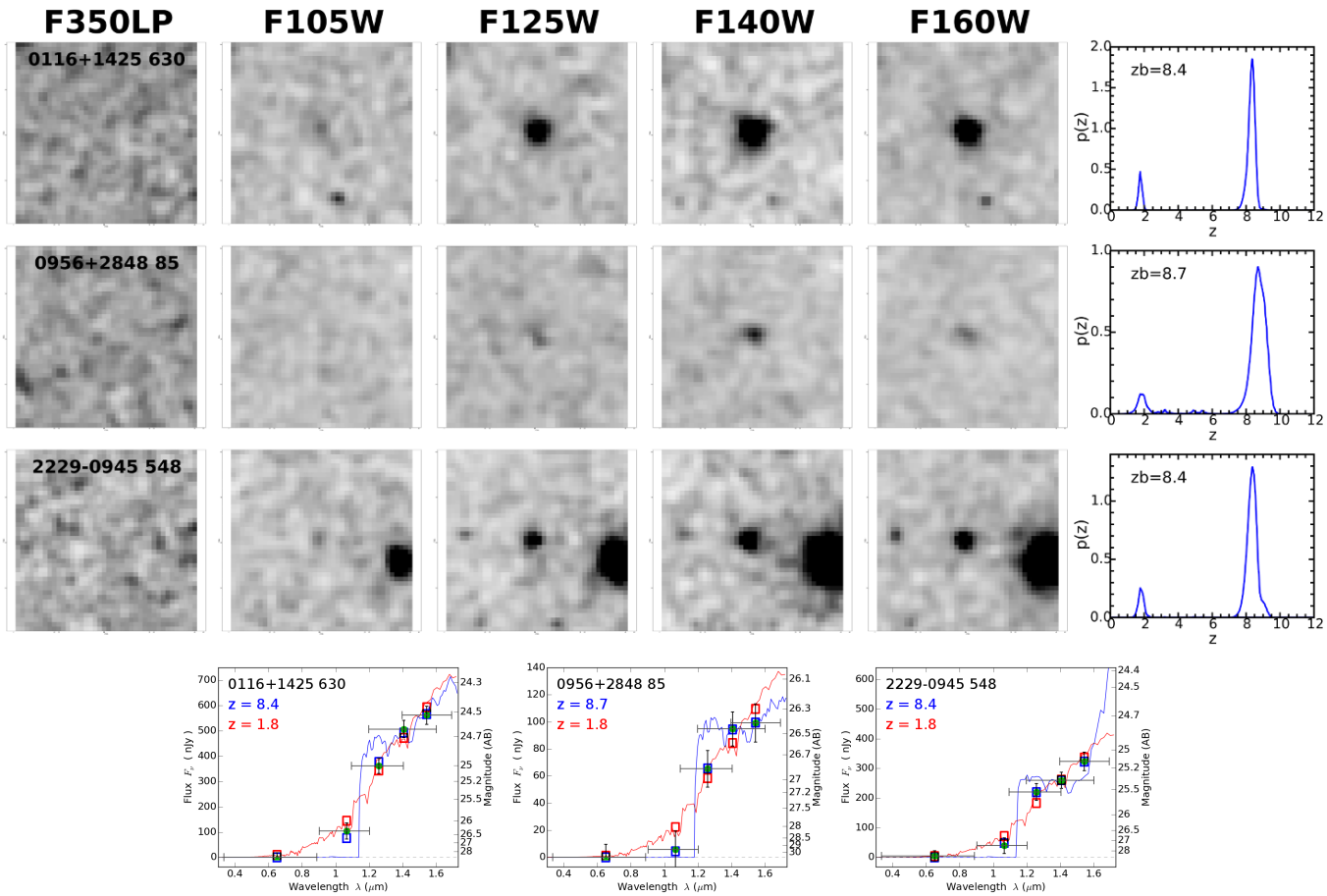

Figure 5. Same as in Figure 4, but for the Y_{105}-JH_{140} dropout candidates listed in Table 2.

borg_2140+0241_37 is comparably bright (H_{160}=24.94) to borg_2134-0708_774, and it is only detected in the two reddest bands of the survey. Therefore, the photometric redshift has a strong preference for $z > 10$ solutions. Like borg_2134-0708_774, this object is also close in projection (1.″02 center to center) to a foreground brighter galaxy (H_{160}=24.05), also expected to be at $z \gtrsim 0.5$ because of the compact size, and therefore a potential lens. The lensing magnification predicted by our modeling is $\mu = 1.2 \pm 0.1$, essentially identical to that for borg_2134-0708_774 (see above), because the smaller angular separation compensates for the lower luminosity of the lensing galaxy. The dropout galaxy has an extended structure, especially in the H_{160}-band image ($r_e = 0.''37$). Such spatial extension of the source is larger than that expected for a typical $z \sim 10$ candidate ($r_e \lesssim 0.''2$), although still marginally smaller than confirmed low-z contaminants in CANDELS ($r_e \gtrsim 0.''4$; see Holwerda et al. 2015).

5.2. Y_{105}-JH_{140} *dropouts*

The Lyman break selection for Y_{105}-JH_{140} dropouts peaks at $z = 8.72$, with a 95% confidence region from $z = 7.75$ up to $z = 9.68$ (see Figure 3). We identify three candidates with postage stamps and p(z) shown in Figure 5, all with the most likely redshift at or below the theoretical median of the distribution. However, not only is the sample size very small, but a skewed distribution is expected when the galaxy LF evolves rapidly over the redshift range covered by the selection (Muñoz & Loeb 2008).

borg_0116+1425_630 This object is exceptionally bright for a $z > 8$ candidate (H_{160}=24.53 mag, corresponding to $M_{AB} \sim -22.8$). It is detected at high S/N ($S/N_{140} = 12.6$, $S/N_{160} = 16.1$) and has a best photometric redshift solution $z = 8.4$ and compact size ($r_e = 0.''17$ after accounting for the H_{160} PSF). This source is about 0.5 mag brighter than the four $z \geq 7$ candidates in the EGS field presented by Roberts-Borsani et al. (2015), one of which shows an emission line consistent with Lyα at $z = 8.68$ (Zitrin et al. 2015; and two others have Lyα emission at $z = 7.73$ and $z = 7.48$; see Oesch et al. 2015; Roberts-Borsani et al. 2015). Our new source thus appears an ideal candidate for spectroscopic follow-up, with the potential to elucidate how galaxy formation proceeds for the brightest sources well into the epoch of reionization. The photometric redshift for the galaxy shows two peaks (Figure 5), but the lower redshift ($z \sim 1.8$) early-type SED is disfavored by the current data and by the compact size (see Holwerda et al. 2015). Possibly, part of the emitted flux of such a bright source could hint at the presence of an active galactic nucleus (Oesch et al. 2014).

borg_0956+2848_85 is the Y_{105}-JH_{140} candidate with the highest photometric redshift solution ($z = 8.7$). Despite being relatively faint (H_{160}=26.41) it is confi-

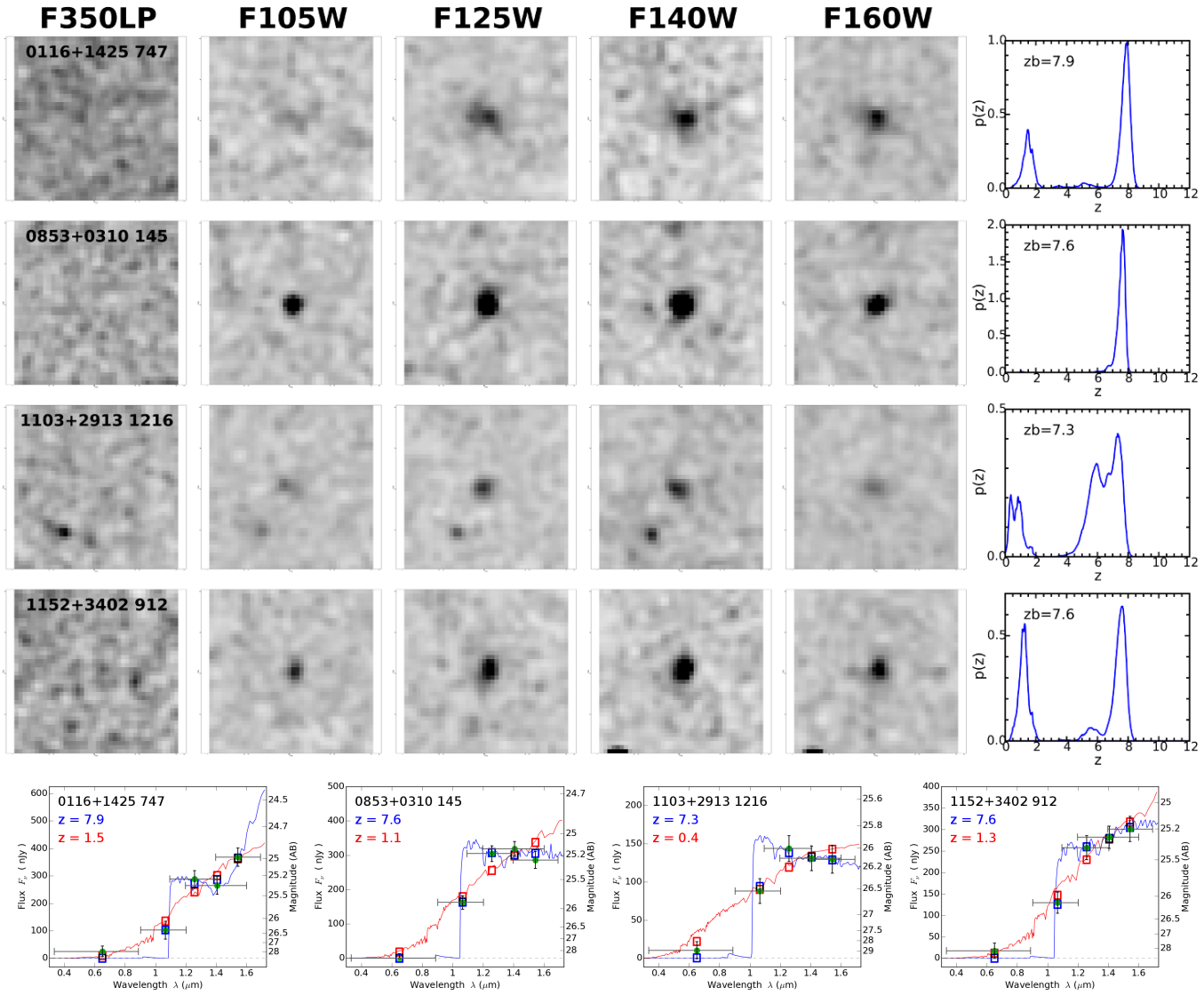

Figure 6. Same as in Figure 4, but for the Y_{105}-J_{125} dropout candidates (see Table 3).

dently detected because of the long exposure times (e.g., 4400s in H_{160}). The Y_{105}-JH_{140} drop is also the most prominent in the sample (Y_{105}-JH_{140}= 2.1). Finally, its compact size ($r_e = 0\farcs08$ after accounting for the H_{160} PSF) strengthens the rejection of the alternative (already disfavored) photometric redshift solution at $z \sim 1.8$.

borg_2229-0945_548 has a very significant drop in F105W (Y_{105}-JH_{140}=2.04), which leads to a photo-z distribution sharply peaked at $z = 8.4$. The dropout galaxy, which has H_{160}= 25.12, is in very close proximity to a brighter $z \sim 2.1$ passive galaxy (H_{160}=22.58; center to center distance equal to $1\farcs48$, see bottom panel in Figure 5). Based on modeling of the foreground deflector following Barone-Nugent et al. (2015) and Mason et al. (2015b), we estimate a gravitational lensing magnification of the dropout flux $\mu \sim 1.3 \pm 0.3$ or $\mu \sim 1.9 \pm 0.7$, respectively.

5.3. Y_{105}-J_{125} *dropouts*

While we optimized BoRG[z9-10] for searching objects at $z > 8$, the multi-band nature of the survey allows us to augment the sample of $z \sim 7-8$ objects as well. We identify candidates in this redshift range as Y_{105}-J_{125} dropouts. Four galaxies satisfy the selection requirements, with a wide range of luminosities ($m_{AB} \sim 25-26.1$ in the H_{160}-band). As shown in Figure 6, the best photometric redshift solutions lie in the range $7.3 < z < 8.0$. One caveat to this selection is that, unlike the earlier BoRG[z8] survey, which relied on the medium-band filter F098M for Y-band imaging, the use of F105W implies a partial overlap with F125W, resulting in a potentially higher contaminant fraction for Y_{105}-J_{125} LBGs (Stanway et al. 2008). However, the analysis of the size distribution of the sample appears reassuring because all four objects have $r_e \leq 0\farcs25$, and only one has $r_e > 0\farcs2$ after accounting for the PSF shape. Thus we have confidence that even in absence of longer wavelength observations and despite the partial overlap of F105W with F125W, the purity of the sample that we

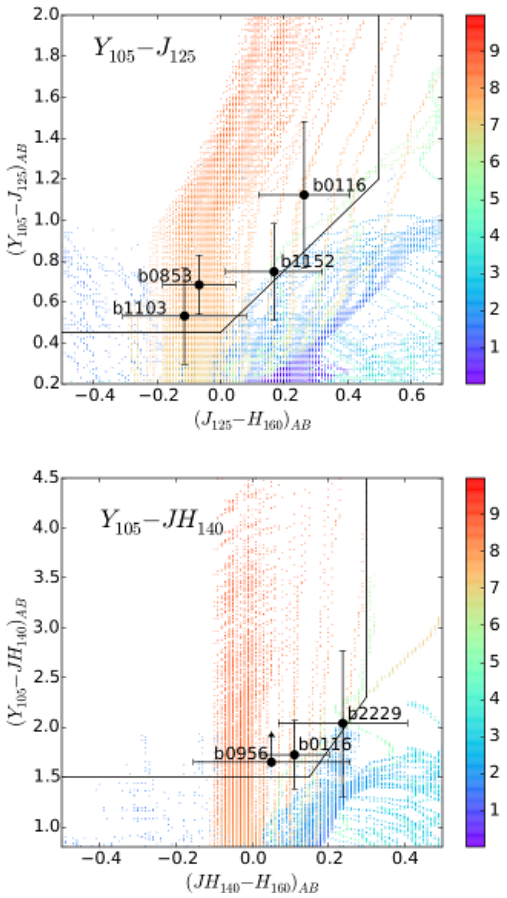

Figure 7. Top panel: Y_{105}-J_{125} dropouts (black filled circles) in the J_{125}-H_{160} versus Y_{105}-J_{125} color-color plot. The upper left region indicates our selection box. The colored marks show were simulated galaxies at different redshift (see color-bar for values) lie. Bottom panel: Same as in the top panel, but for the Y_{105}-JH_{140} dropout sources. Colors are calculated from SExtractor isophotal magnitudes (MAG_ISO).

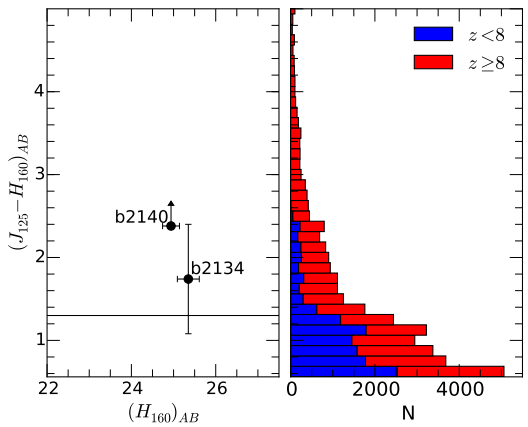

Figure 8. Left panel: J_{125}-JH_{140} dropouts (black filled circles) in the J_{125}-H_{160} versus H_{160}-band magnitude plot. The J_{125}-H_{160} color is calculated from SExtractor isophotal magnitudes (MAG_ISO). Right panel: distribution of the J_{125}-H_{160} color for synthetic galaxies at $z > 8$ (red) and $z < 8$ (blue), showing that the color-cut J_{125}-H_{160}> 1.3 effectively rejects the large majority of contaminants.

constructed is high (see Section 6.2).

6. NUMBER DENSITY AND LUMINOSITY FUNCTION OF BRIGHT LBGS AT $Z \gtrsim 8$

One of the key science drivers of BoRG[z9-10] is to characterize the number density of bright ($L > L_*$) galaxies at $z > 8$. In the initial 25% of the survey, which is presented in this paper, we identified bright, but rare candidates (five in total at $z \sim 8.5$ and $z \sim 10$; see Section 5). These detections translate into preliminary limits of the galaxy number density and UV LF after quantifying the completeness of our search and estimating of the contamination rate.

6.1. *Completeness and selection functions*

Following the prescription of Oesch et al. (2007, 2009, 2012), we ran simulations of artificial source recovery to derive the completeness function, $C(m)$, and magnitude-dependent redshift selection function, $S(z, m)$, at $z \sim 9$ and $z \sim 10$ for each BoRG[z9-10] field. A detailed discussion of the simulations is presented by Oesch et al. (2012) (see also Bradley et al. 2012; Schmidt et al. 2014a for previous applications of the method to the BoRG[z8] survey). To summarize the method, artificial sources with a range of input magnitudes, sizes, spectral energy distributions, and redshifts are added to the science images. Then dropout catalogs are constructed following the steps described in Sections 3.2 and 4. From these catalogs we construct the completeness $C(m)$ and source selection $S(z, m)$ functions. The procedure is carried out for each individual field (see Figure 9 for borg_0116+1425 field, representative of all those in our dataset). The sum of all completeness weighted selection functions, integrated over redshift, then determines the effective comoving volume probed as a function of source brightness:

$$V_{\rm eff}(m) = \int_0^\infty S(z,m)C(m)\frac{dV}{dz}dz$$

$V_{\rm eff}(m)$ takes into account all aspects of the selection of high-z sources, including (1) loss of volume due to foreground sources and/or areas affected by persistence; (2) decreased detection efficiency as the survey magnitude limit is approached; (3) effects of photometric scatter which can move artificial sources at high-z outside the parameter space for selection. $V_{\rm eff}(m)$ is shown in Figure 9, from which it is immediately clear that the recovery efficiency of BoRG[z9-10] drops around $m_{AB} = 26.2$ in the H_{160}-band for sources detected at $S/N \geq 8$. At bright magnitudes, the effective volume of the search for the $z \sim 9$ and $z \sim 10$ samples is respectively $(2.5-3.5)\times10^5$ Mpc^3 comoving.

6.2. *Contamination*

Catalogs of high-z candidates selected from broadband imaging are potentially affected by contamination of low-z interlopers with similar colors, which may be Galactic stars, low/intermediate redshift galaxies, or spurious sources (Bouwens et al. 2015b).

In general stellar contamination is not a significant source of concern for resolved sources detected at $S/N \gtrsim 10$, since in that case the `SExtractor` CLASS_STAR parameter can reliably discriminate between stars and galaxies (Bouwens et al. 2015b). All sources in our main samples have CLASS_STAR< 0.5 (see Table 2), which is comfortably different from CLASS_STAR> 0.9 typically

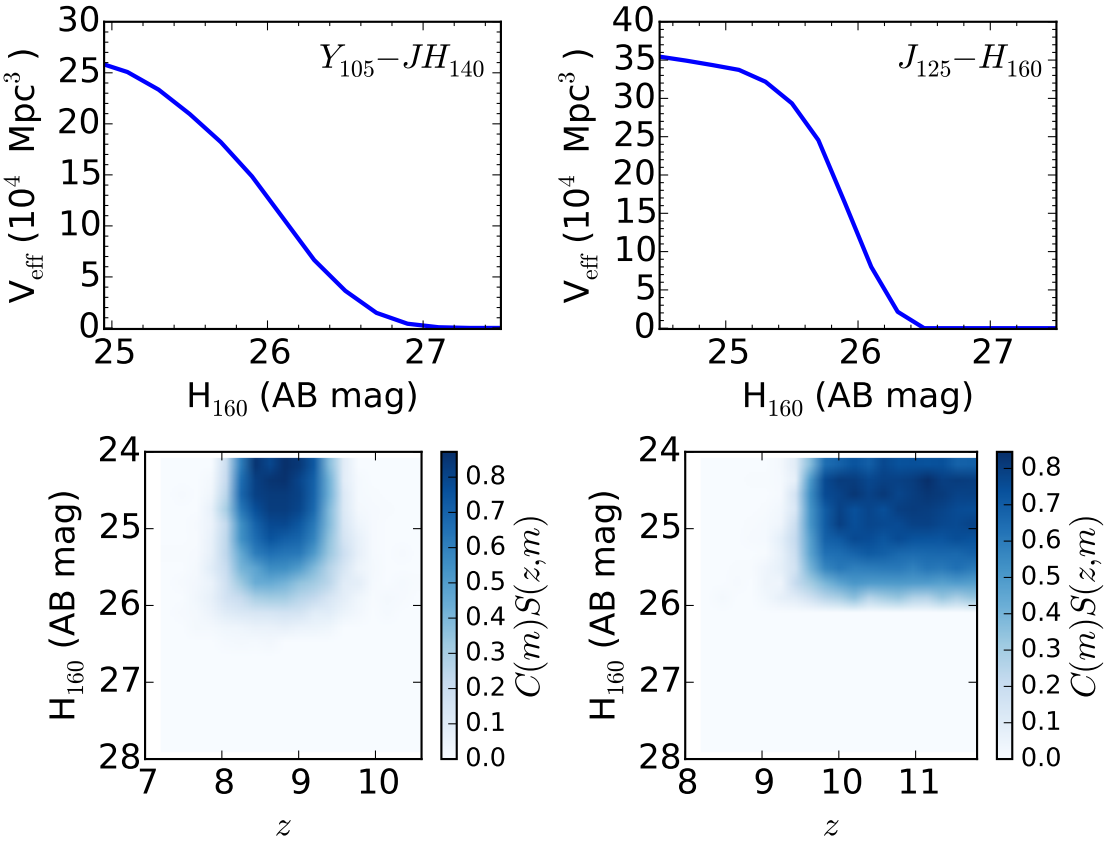

Figure 9. Top panels: Effective comoving volume $V_{\rm eff}$ in Mpc^3 as a function of the H_{160}-band magnitude for our selection of LBGs as Y_{105}-JH_{140} (left panel) and J_{125}-H_{160} dropouts (right panel). Bottom panels: Plot of the selection function $S(z,m)$ for the Y_{105}-JH_{140} (left panel) and J_{125}-H_{160} dropout (right panel) samples obtained for the field borg_0116+1425 representative of a typical BoRG[z9-10] pointing. $S(z,m)$ was derived from simulations, recovering artificial sources inserted in the images (Oesch et al. 2007, 2009, 2012).

measured for point sources. In addition, stars with red IR colors have a surface density that remains relatively flat in the magnitude range $21 \lesssim m_{AB} \lesssim 26$ (Holwerda et al. 2014).

The color-color criteria we adopted for the selection of Y_{105}-JH_{140} and J_{125}-H_{160} dropouts exclude the contamination from dwarf stars based on the colors of these sources. On the other hand, the sample of Y_{105}-J_{125} dropouts is potentially contaminated by cold red stars. From archival near-IR *HST* datasets (Ryan et al. 2011; Holwerda et al. 2014), we estimate that $n \sim 2$ T-dwarf stars may enter our selection box within the current survey area. From the values of CLASS_STAR and r_e for Y_{105}-J_{125} dropouts we conclude that only borg_0835+0310_145 is compact enough to be a potential stellar interloper of the $z \sim 7.5$ dropout sample.

We do not expect that contamination by spurious sources is a concern because of our requirement of $S/N > 8$ in the detection images combined with stringent color cuts. Schmidt et al. (2014a) analyzed BoRG[z8] data to characterize the noise distribution, and found that on average, one spurious source for each WFC3 pointing is detected at $S/N > 8$ because of hot pixels or detector persistence. However, the colors of these spurious sources are not as red as $z > 8$ dropouts because hot pixels or persistence affect all IR bands. In fact, Schmidt et al. (2014a) found that no spurious source was identified as a dropout within the 350 arcmin^2 of the full BoRG[z8] dataset. Applying the conclusions of that study to the BoRG[z9-10] data analyzed here, we expect $n \lesssim 0.3$ spurious sources in our samples. Note also that since images in all filters are acquired for each pointing in a single visit (lasting less than 8 hours), contamination by transients such as supernova events is negligible since only a $z > 8$ event would have the right colors to enter into our selection.

Finally, we discuss the most significant source of contamination: foreground galaxies with colors similar to $z > 8$ sources. Two main classes of objects may enter our LBG selection: intermediate-age galaxies at $z \sim 1-3$ with a prominent Balmer break, and strong line emitters, which have IR broadband flux dominated by nebular lines (e.g. Hα, [O II], and ø3; Atek et al. 2011; Pacifici et al. 2015) and an undetected faint continuum flux at optical wavelengths (Bouwens et al. 2015b). Spectroscopic follow-up of $z \sim 8$ dropouts in BoRG[z8] has found no evidence of strong emitters after targeting 15 sources (Treu et al. 2012, 2013; Barone-Nugent et al. 2015) selected from ~ 350 arcmin^2. Even more stringently, Bouwens et al. (2015b) estimate that the extreme line emitters capable of contaminating a dropout sample at $z \sim 8$ have a density of $\sim 10^{-3}$ arcmin^{-2}. We thus estimate that extreme line emission is not a significant concern, although

one caveat is that the only $z \gtrsim 10$ candidate identified in UDF field may be an ø3 emitter at $z \sim 2.2$ (see Brammer et al. 2013). The primary source of contaminants in our sample are thus expected to be intermediate redshift galaxies with a strong Balmer break. Estimating the precise contamination fraction from these sources is very challenging, but we expect it to be in the range of $\sim 30\%$ based on the analysis of spectral templates. This figure is comparable to previous estimates of the BoRG[z8] sample purity at the $20-30\%$ level (Trenti et al. 2011; Bradley et al. 2012; Schmidt et al. 2014a). This rate is larger than the typical contamination rate $\lesssim 10\%$ found in Lyman-break samples from legacy fields such as HUDF and CANDELS, that have extensive multi-observatory coverage (Bouwens et al. 2015b). In the absence of observations with Spitzer/IRAC which would help to discriminate between intermediate-z ellipticals and $z > 8$ starbursts, it is possible to use size as a proxy for the H_{160}-[4.5] color (Holwerda et al. 2015), and reassuringly our dropouts sources are generally too compact to be contaminants. One caveat is that the size proxy is unable to discriminate against contamination from sources with unusual colors at $z \sim 6-7$, since they would be similarly compact. Of course, the availability of observations over a wider range of wavelengths would help to identify the presence, if any, of such population in our samples.

The presence of a non-negligible, but not overwhelmingly large contamination fraction can be inferred from the analysis of the redshift probability distribution for the candidates in our sample, as well. For sources at $z \sim 10$, we measure that the probability of being at $z < 8$ is $p = 39\%$, while for $z \sim 9$ dropouts the photo-z estimates are more peaked at high redshift, and there is only an average probability $p = 11\%$ for the candidates to be at $z < 7$. These estimates are in agreement with the study by Pirzkal et al. (2013), where a $\sim 21\%$ contamination fraction is derived for typical samples of galaxies at $8 < z < 12$ identified from *HST* imaging.

Combining all the different approaches to the contamination issue, we assume 30% as baseline estimate of the contamination rate, which is close to the weighted average from the photo-z $[(0.39 \times 3 + 0.11 \times 2)/5 \sim 0.28]$. Thus, we would expect that one to two of the five sources reported in this paper may be low-redshift interlopers.

6.3. *Determination of the luminosity function*

Combining the effective volume and contamination estimates, we derive a step-wise LF for the $z \sim 9$ and $z \sim 10$ samples, which we report in Table 4 and plot in Figure 10. The determination is severely limited by the large Poisson uncertainty, but the comparison with existing constraints on the LF, shown as gray points in the Figure, is informative. Our determination of the bright end of the $z \sim 9$ luminosity function is consistent with the latest measurement by Bouwens et al. (2015a) at $M_{AB} > -21.5$, and at $M_{AB} = -22.2$ the measured number density of $3.7^{+8.3}_{-3.1} \times 10^{-6}\mathrm{Mpc}^{-3}\mathrm{mag}^{-1}$ is within the predictions of the LF model of Mason et al. (2015a), which is successful in describing the LF evolution with redshift. The striking difference with previous searches and with theoretical predictions is the detection of the exceptionally bright candidate borg_0116+1425_630, which if confirmed, would argue against an exponential decline at the bright end and point instead of a power-law LF. One possibility is, of course, that such object is a contaminant, but intriguingly the recent spectroscopic confirmation at $z \sim 8.7$ of a $m_{AB} \sim 25$ source (Zitrin et al. 2015) may suggest that intense starbursts of the order of $50\ \mathrm{M}_{\odot}\mathrm{yr}^{-1}$ could become relatively more common as the redshift increases, and merger driven activity increases over smooth gas accretion.

At $z \sim 10$, the situation is similar. At face value, our LF determination appears too high compared to expectations for objects with $m_{AB} < 25.5$. One possibility to explain our results would be significant lensing magnification, because both candidates are close in proximity to brighter foreground sources. At the current stage and without follow-up studies of the two candidates to increase the confidence on their $z \sim 10$ nature, it is difficult to draw firmer conclusions. Of course, the full BoRG[z9-10] dataset will allow us to investigate whether this initial overabundance of very bright candidates is confirmed or not and to systematically account for the effect of lensing magnification on the LF via Bayesian methods (Schmidt et al. 2014a; Mason et al. 2015b).

As an additional consistency check for the number of detections reported here compared to theoretical expectations, we estimated the number density by integrating the Mason et al. (2015b) LF model (see also Trenti et al. 2010; Tacchella et al. 2013) over the effective volume of the survey. For $z \sim 9$, we estimate a total of $\langle n \rangle = 1.1^{+1.5}_{-0.7}$ detections, consistent with the $n = 2.1$ observed after accounting for 30% contamination. For $z \sim 10$, the expectation is $\langle n \rangle = 0.1^{+0.25}_{-0.08}$ detections, so this is in mild ($\sim 2\sigma$) tension with the observed number after accounting again for 30% contamination. If compared to expectations from the $z \sim 8$ LF, which would predict $\langle n \rangle \sim 11$ detections in the survey, our result of an contamination-corrected sample size of $n \sim 3.5$ sources indicates a decline in bright galaxies with increasing redshift, confirming the clear trend previously established observationally and by theoretical modeling (e.g., Oesch et al. 2012; Bouwens et al. 2015b; Mason et al. 2015a).

Finally, regarding the sample of four objects at $z \sim 7.3-8$, we defer the study of the LF until the full dataset has been acquired, since the new area (~ 130 arcmin^2) is only a modest improvement over the existing BoRG[z8] data (~ 350 arcmin^2) and the determination from the combination of all *HST* archival data (~ 1000 arcmin^2; Bouwens et al. 2015a).

7. CONCLUSION

In this paper we presented the design and initial results of the BoRG[z9-10] survey, a large (480 orbits) pure-parallel imaging program with *HST*/WFC3 which is acquiring medium depth ($m_{AB} \sim 27$, 5σ point source), random pointing imaging at optical and infrared wavelengths over a total of ~ 550 arcmin^2, divided among more than 100 independent lines of sight (GO13767, PI Trenti). The primary goal of BoRG[z9-10] is the detection of $L > L_*$ galaxy candidates at $z > 8$ taking advantage of the large number of independent lines of sight to minimize the impact of cosmic variance.

The key results are the following:

- Through an optimized design of the pure-parallel

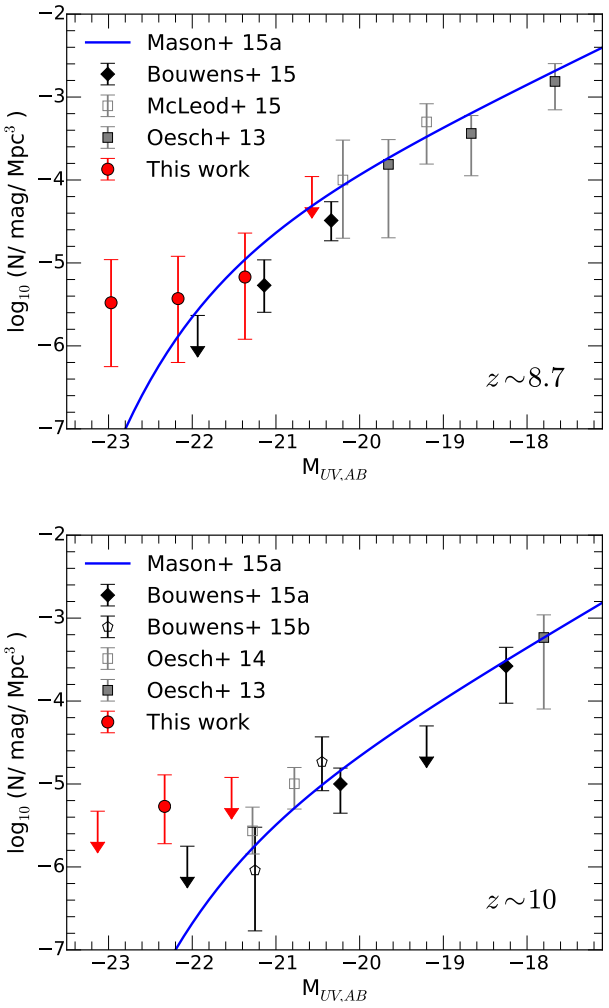

Figure 10. Step-wise determinations of the UV LF at $z \sim 8.7$ (top panel) and $z \sim 10$ (bottom panel), without magnification lensing corrections. The red filled circles and upper limits refer to this paper, other symbols to Oesch et al. (2013, 2014); Bouwens et al. (2015a,b); McLeod et al. (2015) as labeled. The over-plotted blue line indicates the galaxy UV luminosity function as from Mason et al. (2015a).

opportunities (Section 2), we have been able to achieve an image quality nearly equivalent to that of primary dithered imaging (Section 3.1 and Figure 2).

- From the initial $\sim$ 25% of the survey, we identified five very bright galaxy candidates at $z > 8.3$ with $m_{AB} \sim 24.5-26.5$ detected at $S/N > 8$, contributing significantly to increase the small sample sizes of intrinsically bright objects identified at $z > 8$ from legacy fields (Bouwens et al. 2015a,b). To select the objects we resorted to a combination of color selection (LBG technique; see Steidel et al. 1996) and Bayesian photometric redshift estimates, with the candidate properties presented in Section 5 and in Figures 4 and 5.

- One source, borg_0116+1425_630, is exceptionally bright, with H_{160}=24.5 and best photometric redshift $z = 8.4$, implying $M_{AB} = -22.75$ and a star formation rate (SFR) of $\sim 66\,M_\odot yr^{-1}$. The existence of such a bright source at $z > 8$, if confirmed, would be a major indication that galaxy formation at early times can undergo phases of rapid bursts with sustained SFR, possibly because of frequent major mergers.

- After accounting for completeness corrections and for a modest contamination rate (Section 6.2), the inferred number density is consistent with previous observations and theoretical modeling (e.g., Bouwens et al. 2015b; Mason et al. 2015b), although our brightest bins at $z \sim 9$ and $z \sim 10$ have an excess compared to expectations (Figure 10). However, the excess might be explained with small number fluctuations, since the number counts predictions are not significantly different. For example, we observe three sources at $z \sim 9$ versus the expectation of $\langle n \rangle = 1.1$. One additional contributing factor could be line-of-sight gravitational lensing since some of our candidates are in close proximity with brighter and more massive foreground sources (see Mason et al. 2015b; Barone-Nugent et al. 2015).

Overall, our new candidates, and in particular borg_0116+1425_630, are ideal for follow-up observations either with Spitzer/IRAC to measure the rest-frame optical light and improve sample purity[26], or with near-IR spectroscopy. The prospects for the latter to succeed are favorable based on the recent report of detection of Lyα in a comparably bright source by Zitrin et al. 2015.

The evolution of the bright end of the galaxy LF into the epoch of reionization is an active topic of research, with potential to elucidate when and how the feedback processes that affect the brightest galaxies at lower redshift come in place. The current status of the field is somewhat unclear, with some tension between ground-based determinations at $z \sim 7$, which suggest a power-law fall-off rather than a Schechter function at the bright end (Bowler et al. 2014), while $z \sim 8$ data from *HST* prefer an exponential cut-off, including the large area determination from our previous BoRG[z8] survey (Schmidt et al. 2014a; but see Finkelstein et al. 2015 for support to a comparably good fit with a single power law). Our preliminary results reported here at $z > 8$ are not conclusive, but the full dataset which is being acquired will improve the constraints with an increase of a factor four in area. Finally, when combined with other ongoing programs that will find bright (lensed) high-z candidates, such as GLASS (GO13459, PI. T. Treu, Schmidt et al. 2014b; Treu et al. 2015) and RELICS (GO14096, PI. D. Coe), BoRG[z9-10] will contribute to create a legacy set of near-IR observations from which the most promising spectroscopic targets for early *JWST*/NIRSPEC observations can be selected.

We thank Camilla Pacifici and Robert Barone-Nugent for useful discussions and the anonymous referee for valuable comments. This work was partially supported by grants *HST*/GO 13767, 12905, and 12572.

[26] Our team has been awarded time for follow-up of the $z \sim 9-10$ candidates presented in this paper after submission of the manuscript. These Spitzer observations (Program 12058, PI. R. J. Bouwens) will be carried out by the end of 2016.

Facilities: *HST*(WFC3).

REFERENCES

Anderson, J. 2014, The Impact of x-CTE in the WFC3/UVIS detector on Astrometry, Tech. rep.
Atek, H., Siana, B., Scarlata, C., et al. 2011, ApJ, 743, 121
Barone-Nugent, R. L., Wyithe, J. S. B., Trenti, M., et al. 2015, MNRAS, 450, 1224
Barone-Nugent, R. L., Trenti, M., Wyithe, J. S. B., et al. 2014, ApJ, 793, 17
Benítez, N. 2000, ApJ, 536, 571
Benitez, N., Dupke, R., Moles, M., et al. 2014, ArXiv e-prints, arXiv:1403.5237
Bertin, E., & Arnouts, S. 1996, A&AS, 117, 393
Bouwens, R. J., Illingworth, G. D., Franx, M., & Ford, H. 2008, ApJ, 686, 230
Bouwens, R. J., Illingworth, G. D., González, V., et al. 2010, ApJ, 725, 1587
Bouwens, R. J., Illingworth, G. D., Oesch, P. A., et al. 2012, ApJ, 752, L5
Bouwens, R. J., Oesch, P. A., Labbé, I., et al. 2015a, ArXiv e-prints, arXiv:1506.01035
Bouwens, R. J., Illingworth, G. D., Oesch, P. A., et al. 2015b, ApJ, 803, 34
Bowler, R. A. A., Dunlop, J. S., McLure, R. J., et al. 2014, MNRAS, 440, 2810
Bradley, L. D., Bouwens, R. J., Ford, H. C., et al. 2008, ApJ, 678, 647
Bradley, L. D., Trenti, M., Oesch, P. A., et al. 2012, ApJ, 760, 108
Bradley, L. D., Zitrin, A., Coe, D., et al. 2014, ApJ, 792, 76
Brammer, G., Pirzkal, N., McCullough, P., & MacKenty, J. 2014, Time-varying Excess Earth-glow Backgrounds in the WFC3/IR Channel, Tech. rep.
Brammer, G. B., van Dokkum, P. G., Illingworth, G. D., et al. 2013, ApJ, 765, L2
Casertano, S., de Mello, D., Dickinson, M., et al. 2000, AJ, 120, 2747
Coe, D., Benítez, N., Sánchez, S. F., et al. 2006, AJ, 132, 926
Coe, D., Bradley, L., & Zitrin, A. 2015, ApJ, 800, 84
Coe, D., Zitrin, A., Carrasco, M., et al. 2013, ApJ, 762, 32
Ellis, R. S., McLure, R. J., Dunlop, J. S., et al. 2013, ApJ, 763, L7
Fialkov, A., & Loeb, A. 2015, ApJ, 806, 256
Finkelstein, S. L., Papovich, C., Dickinson, M., et al. 2013, Nature, 502, 524
Finkelstein, S. L., Ryan, Jr., R. E., Papovich, C., et al. 2015, ApJ, 810, 71
Finlator, K., Oppenheimer, B. D., & Davé, R. 2011, MNRAS, 410, 1703
Fioc, M., & Rocca-Volmerange, B. 1997, A&A, 326, 950
Gonzaga, S. e. a. 2012, The DrizzlePac Handbook
González, V., Labbé, I., Bouwens, R. J., et al. 2010, ApJ, 713, 115
Grogin, N. A., Kocevski, D. D., Faber, S. M., et al. 2011, ApJS, 197, 35
Holwerda, B. W., Bouwens, R., Oesch, P., et al. 2015, ApJ, 808, 6
Holwerda, B. W., Trenti, M., Clarkson, W., et al. 2014, ApJ, 788, 77
Illingworth, G. D., Magee, D., Oesch, P. A., et al. 2013, ApJS, 209, 6
Koekemoer, A. M., Faber, S. M., Ferguson, H. C., et al. 2011, ApJS, 197, 36
Koekemoer, A. M., Ellis, R. S., McLure, R. J., et al. 2013, ApJS, 209, 3
Labbé, I., Oesch, P. A., Illingworth, G. D., et al. 2015, ApJS, 221, 23
Mason, C. A., Trenti, M., & Treu, T. 2015a, ApJ, 813, 21
Mason, C. A., Treu, T., Schmidt, K. B., et al. 2015b, ApJ, 805, 79
McLeod, D. J., McLure, R. J., Dunlop, J. S., et al. 2015, MNRAS, 450, 3032
McLure, R. J., Dunlop, J. S., Bowler, R. A. A., et al. 2013, MNRAS, 432, 2696
Muñoz, J. A., & Loeb, A. 2008, MNRAS, 385, 2175
Noeske, K., Baggett, S., Bushouse, H., et al. 2012, WFC3 UVIS Charge Transfer Eciency October 2009 to October 2011, Tech. rep.
Oesch, P. A., Stiavelli, M., Carollo, C. M., et al. 2007, ApJ, 671, 1212
Oesch, P. A., Carollo, C. M., Stiavelli, M., et al. 2009, ApJ, 690, 1350
Oesch, P. A., Bouwens, R. J., Illingworth, G. D., et al. 2012, ApJ, 759, 135
—. 2013, ApJ, 773, 75
—. 2014, ApJ, 786, 108
Oesch, P. A., van Dokkum, P. G., Illingworth, G. D., et al. 2015, ApJ, 804, L30
Oke, J. B., & Gunn, J. E. 1983, ApJ, 266, 713
Pacifici, C., da Cunha, E., Charlot, S., et al. 2015, MNRAS, 447, 786
Pentericci, L., Vanzella, E., Fontana, A., et al. 2014, ApJ, 793, 113
Pirzkal, N., Rothberg, B., Ryan, R., et al. 2013, ApJ, 775, 11
Planck Collaboration, Ade, P. A. R., Aghanim, N., et al. 2015, ArXiv e-prints, arXiv:1502.01589
Postman, M., Coe, D., Benítez, N., et al. 2012, ApJS, 199, 25
Rafelski, M., Teplitz, H. I., Gardner, J. P., et al. 2015, AJ, 150, 31
Roberts-Borsani, G. W., Bouwens, R. J., Oesch, P. A., et al. 2015, ArXiv e-prints, arXiv:1506.00854
Robertson, B. E. 2010, ApJ, 713, 1266
Ryan, R. E., Thorman, P. A., Yan, H., et al. 2011, ApJ, 739, 83
Schechter, P. 1976, ApJ, 203, 297
Schenker, M. A., Robertson, B. E., Ellis, R. S., et al. 2013, ApJ, 768, 196
Schlafly, E. F., & Finkbeiner, D. P. 2011, ApJ, 737, 103
Schmidt, K. B., Treu, T., Trenti, M., et al. 2014a, ApJ, 786, 57
Schmidt, K. B., Treu, T., Brammer, G. B., et al. 2014b, ApJ, 782, L36
Stanway, E. R., Bremer, M. N., & Lehnert, M. D. 2008, MNRAS, 385, 493
Stark, D. P., Ellis, R. S., Chiu, K., Ouchi, M., & Bunker, A. 2010, MNRAS, 408, 1628
Steidel, C. C., Adelberger, K. L., Giavalisco, M., Dickinson, M., & Pettini, M. 1999, ApJ, 519, 1
Steidel, C. C., Giavalisco, M., Pettini, M., Dickinson, M., & Adelberger, K. L. 1996, ApJ, 462, L17
Stiavelli, M. 2009, From First Light to Reionization: The End of the Dark Ages
Su, J., Stiavelli, M., Oesch, P., et al. 2011, ApJ, 738, 123
Tacchella, S., Trenti, M., & Carollo, C. M. 2013, ApJ, 768, L37
Trenti, M., & Stiavelli, M. 2008, ApJ, 676, 767
Trenti, M., Stiavelli, M., Bouwens, R. J., et al. 2010, ApJ, 714, L202
Trenti, M., Bradley, L. D., Stiavelli, M., et al. 2011, ApJ, 727, L39
—. 2012, ApJ, 746, 55
Treu, T., Schmidt, K. B., Trenti, M., Bradley, L. D., & Stiavelli, M. 2013, ApJ, 775, L29
Treu, T., Trenti, M., Stiavelli, M., Auger, M. W., & Bradley, L. D. 2012, ApJ, 747, 27
Treu, T., Schmidt, K. B., Brammer, G. B., et al. 2015, ApJ, 812, 114
van Dokkum, P. G. 2001, PASP, 113, 1420
Vanzella, E., Fontana, A., Pentericci, L., et al. 2014, A&A, 569, A78
Wuyts, S., Labbé, I., Schreiber, N. M. F., et al. 2008, ApJ, 682, 985
Wyithe, J. S. B., Yan, H., Windhorst, R. A., & Mao, S. 2011, Nature, 469, 181
Zitrin, A., Labbé, I., Belli, S., et al. 2015, ApJ, 810, L12

APPENDIX

APPENDIX A- OTHER POSSIBLE HIGH-Z CANDIDATES

In this Appendix we briefly investigate and present results on the search for high-z sources in the dataset based on alternative criteria. In addition, we report the candidates that passed the Lyman break color selection for $z > 8$

sources, but were removed from the main sample because their Bayesian photometric redshift indicated a best solution at $z < 7$. Overall, we discuss six additional high-z candidates, with four of them being possible/likely contaminants because of a preferred low-z solution in the photometric redshift distribution. Four of the six sources arise from the use of F160W as sole detection image (rather than the combination of F140W and F160W). One candidate is excluded from the main sample because of the low-z peak in $p(z)$. Finally, one additional candidate is identified by adopting the Bouwens et al. (2015b) selection for $z \sim 8$ sources (but would have been excluded from the main sample in any case because of a preferred low-z photometric redshift solution).

Additional candidates from F160W-only catalogs

Catalogs constructed using F160W-only as detection image have been processed to search for candidates at $z > 7$ following the main text analysis based on F140W+F160W selection. We identified three new sources at $z > 7$, that were not included in the main samples because of slightly different colors or because a hot pixel was present within their segmentation maps. Interestingly, one of these new candidates, borg_1209+4543_1696, is identified as a Y_{105}-JH_{140} dropout, with a photometric redshift distribution strongly peaked at $z = 8.56$ and $H_{160} \sim 25.0$. The reason why the source is not in the main catalog is because of the presence of an hot pixel, correctly identified by the reduction pipeline, in the outskirts of the dropout image. The pixel is included in the segmentation map of the F160W+F140W detection image, thereby excluding the galaxy from further analysis owing to our choice to discard any source with one or more pixels having zero weight (infinite rms). With the selection in F160W only, the galaxy segmentation map avoids inclusion of the hot pixel, and `SExtractor` photometry is performed without incurring in unbound errors. Since the defect is located in the outer parts of the image of the galaxy, we consider this source a credible high-z candidate, albeit its relatively large size would indicate the possibility that the low-z solution is preferred. The other two sources are less interesting and have a high probability of being contaminants, with colors near/at the boundary of the selection region.

Search for sources with Bayesian photometric redshift at $z > 7$

We analyzed the photometric redshift probability distribution for each galaxy in our catalogs, constructed following the procedure introduced in Section 3.3. No new candidates at $z > 7$ have been identified this way.

Candidates with degenerate photo-z solutions

Three sources listed in Table 5 and shown in Figure 11 have a p(z) distribution peaked at $z \sim 1-2$ and magnitudes $H_{160} \sim 25-26.5$. The existing data make it difficult to evaluate whether this is an effect of photometric scatter versus the presence of a population of interlopers with similar near-IR colors, especially because the compact effective radii of these sources would corroborate the high-z photometric solution.

Y_{105}-J_{125} selection following Bouwens et al. (2015b)

The selection of $z \sim 7.5-8$ sources in Section 4 has been optimized for the BoRG[z9-10] filter set. Here, we select sources following the criteria adopted for legacy fields data by Bouwens et al. (2015b), with the main difference being the availability of a larger number of blue (non-detection) bands from surveys such as GOODS/CANDELS (Grogin et al. 2011). The selection criteria are:

$$S/N_{350} < 1.5$$
$$S/N_{125} \geq 6$$
$$S/N_{140} \geq 6$$
$$S/N_{160} \geq 4$$
$$m_{105} - m_{125} > 0.45$$
$$m_{105} - m_{125} > 0.75 \cdot (m_{125} - m_{160}) + 0.525$$
$$m_{125} - m_{160} < 0.5$$

With this selection, we identified one additional Y_{105}-J_{125} dropout borg_0119-3411_22, which is quite bright (H_{160}=25.06). In the near-IR color-color space, the source lies close to the boundaries of the selection box for high-z objects. Therefore, it is not surprising that the photometric redshift distribution shows both a low and an high redshift peak (Figure 11), with the low-z solution marginally preferred. The uncertainty in the nature of this source is compounded by the relatively short exposure time in F350LP which was constrained by readout conflicts with the primary observations associated to this opportunity.

The conclusion from these additional searches is that the failure to identify credible additional candidates both with an alternate color selection, and with a photo-z analysis (Section 3.3), confirms that the selection criteria adopted in the main text are robust.

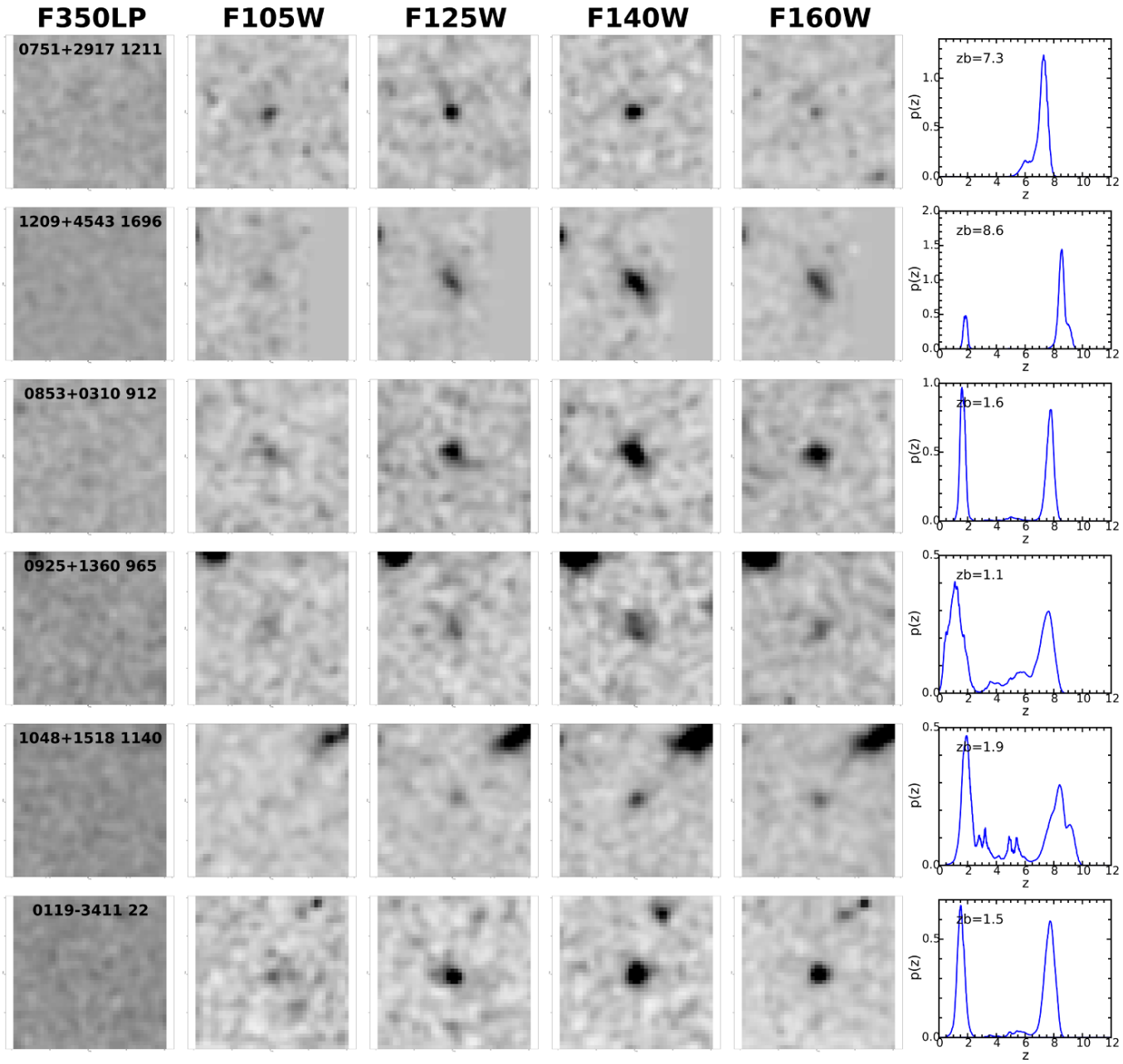

Figure 11. Postage-stamps cutouts and photometric redshift probability distribution p(z) for the additional dropout candidates discussed in the Appendix.

Table 1
BoRG[z9-10] fields coordinates, exposure times, and limiting magnitudes

Field ID	α(J2000) (deg)	δ(J2000) (deg)	# of orbits	E(B-V)	F350LP exp time	F350LP m_{lim}	F105W exp time	F105W m_{lim}	F125W exp time	F125W m_{lim}	F140W exp time	F140W m_{lim}	F160 exp time	F160 m_{lim}	Effective area
borg_0132+3035*	23.11	+30.59	4	0.042	1880		2109		2109		1809		2409		
borg_0133+3043*	23.37	+30.72	4	0.035	1830		2159		2109		1759		2409		
borg_0134+3034*	23.49	+30.58	4	0.037	1860		2159		2109		1759		2409		
borg_0134+3041*	23.43	+30.68	4	0.035	1830		2159		2109		1156		1606		
borg_0116+1425	19.06	+14.41	4	0.035	2095	26.99	2209	26.44	2059	26.57	1759	26.45	2409	26.45	4.40
borg_0119-3411	19.68	-34.18	3	0.023	1306	26.70	1606	26.23	1506	26.17	1306	26.55	1759	26.34	4.27
borg_0337-0507	54.38	-5.12	4	0.038	1967	26.95	2109	26.41	2059	26.49	1709	26.60	2409	26.46	4.42
borg_0554-6005	88.39	-60.09	5	0.049	2252	27.05	2512	26.42	2412	26.81	2059	26.90	2812	26.70	4.12
borg_0751+2917	117.71	+29.28	5	0.037	2210	26.95	2462	26.59	2412	26.60	2009	26.72	2812	26.55	4.43
borg_0853+0310	133.18	+3.16	3	0.043	1392	26.93	1556	26.60	1506	26.50	1256	26.59	1709	26.38	4.49
borg_0925+1360	141.31	+14.00	3	0.027	1510	26.88	1706	26.55	1506	26.48	1306	26.43	1859	26.33	4.52
borg_0925+3439	141.33	+34.65	4	0.017	2039	27.03	2159	26.58	2059	26.57	1759	26.61	2459	26.51	4.47
borg_0953+5157	148.26	+51.95	4	0.008	1809	27.24	2359	26.96	2309	26.83	1959	26.91	2662	26.67	4.44
borg_0956+2848	149.10	+28.80	7	0.016	2940	27.15	3865	26.77	3768	26.78	3215	26.88	4418	26.76	4.43
borg_1015+5945†	153.74	+59.75	3+4	0.009	3084		4215		4018		3468		4718		
borg_1018+0544	154.47	+5.74	4	0.017	2000	27.07	2109	26.61	2009	26.59	1759	26.66	2409	26.52	4.44
borg_1048+1518	161.97	+15.30	3+4	0.024	2478	27.15	3112	26.89	2912	26.80	2512	26.86	3518	26.68	4.43
borg_1048+1518†	161.97	+15.30	4	0.024	1980		2059		1959		1659		2309		
borg_1103+2913	165.68	+29.22	3+3	0.025	2575	27.21	2912	26.83	2812	26.80	2312	26.87	3212	26.73	4.46
borg_1106+3508	166.53	+35.14	5	0.016	2480	27.15	2762	26.63	2662	26.76	2209	26.80	3112	26.65	4.44
borg_1115+2548	168.66	+25.80	4	0.015	2151	27.10	2462	26.80	2412	26.76	2009	26.82	2762	26.63	4.50
borg_1127+2653⋆	171.81	+26.88	3	0.015											
borg_1142+3020	175.62	+30.34	4	0.018	2130	27.19	2159	26.83	2109	26.77	1759	26.79	2409	26.61	4.51
borg_1152+3402	177.91	+34.03	3	0.017	1154	26.88	1456	26.56	1406	26.45	1156	26.57	1606	26.40	4.40
borg_1154+4639	178.44	+46.45	6	0.028	2583	27.38	3412	27.04	3212	26.90	2712	27.07	3718	26.83	4.29
borg_1160+0015	179.98	+ 0.25	3	0.028	1473	26.93	1606	26.55	1506	26.48	1256	26.51	1806	26.42	4.48
borg_1209+4543	182.36	+45.72	3+5	0.012	3500	27.46	3918	26.84	3718	27.10	3165	27.15	4421	26.93	4.44
borg_1410+2623	212.41	+26.38	4	0.014	2210	27.22	2462	26.69	2412	26.81	2009	26.90	2812	26.66	4.44
borg_1438-0142	219.45	-1.70	3+5	0.037	3393	27.28	3918	27.01	3768	26.96	3165	27.02	4421	26.84	4.37
borg_1520-2501◇	230.08	-25.02	3	0.142	1872	26.58	1356	26.31	1256	26.27	1006	26.26	1506	26.18	4.28
borg_1525+0955	231.17	+9.92	3	0.034	1230	26.88	1456	26.57	1356	26.48	1156	26.51	1609	26.29	4.31
borg_1525+0960	231.19	+10.00	5	0.033	2154	27.15	2462	26.84	2362	26.77	2009	26.83	2862	26.64	4.23
borg_2134-0708	323.54	-7.13	3+4	0.028	3605	26.90	3715	26.27	3515	26.45	2965	26.48	4168	26.36	4.51
borg_2140+0241	324.89	+2.69	3	0.076	1872	26.94	1406	26.32	1356	26.32	1156	26.50	1606	26.34	4.51
borg_2141-2310*	325.15	-23.17	3	0.042	1350		1556		1406		1256		1709		
borg_2229-0945	337.19	-9.75	3	0.043	1479	26.83	1606	26.37	1506	26.34	1256	26.38	1759	26.25	4.49

NOTE: Column 1: Field name derived from the coordinates. Columns 2-3: α and δ coordinates (in degrees) as from the F140W exposure. Column 4: total number of *HST* orbits allocated. Column 5: Galactic extinction E(B-V) from Schlafly & Finkbeiner (2011). Columns 6-15: exposure time (in seconds) and 5σ limiting magnitude (in AB magnitudes) within a $r = 0\farcs32$ aperture in each band. Column 16: effective area (in arcmin^2).

* Primary and parallel observations targeting M33 (borg_0132+3035, borg_0133+3043, borg_0134+3034, borg_0134+3041) or NGC7099 (borg_2141-2310).

† Images affected by scattered earthlight (see WFC3 Data Hand Book Section 6.10). We are currently building a model to successfully remove the effect from the data.

⋆ Guide star acquisition failure.

◇ High Galactic extinction.

Table 2
BoRG[z9-10] $z \sim 9-10$ candidates

Obj ID	α(J2000) (deg)	δ(J2000) (deg)	H_{160} (AB mag)	M_{AB} (AB mag)	Colors					S/N				r_e	Stellarity	Photo-z
					Y_{105}-J_{125}	J_{125}-H_{160}	Y_{105}-JH_{140}	JH_{140}-H_{160}	F350LP	Y_{105}	J_{125}	JH_{140}	H_{160}			
2134-0708_774	323.5623	-7.1200	25.35±0.26	-22.18±0.26	> 0.37	1.74±0.66	> 1.53	0.59±0.26	1.2	0.0	1.7	5.0	7.7	0.23	0.01	10.0
2140+0241_37	324.8939	+2.6756	24.94±0.20	-22.66±0.20	-	> 2.38	> 1.58	0.79±0.27	-1.2	0.1	-0.3	4.7	8.28	0.37	0.01	10.5
0116+1425_630	19.0347	+14.4026	24.53±0.10	-22.75±0.10	1.36±0.34	0.48±0.11	1.72±0.34	0.11±0.09	-0.2	3.3	13.2	12.6	16.1	0.17	0.03	8.4
0956+2848_85	149.1227	+28.7920	26.41±0.19	-20.91±0.19	1.70±2.60	0.45±0.27	>1.65	0.05±0.21	-0.5	0.4	4.9	7.7	7.2	0.08	0.07	8.7
2229-0945_548	337.1903	-9.7491	25.12±0.17	-22.15±0.17	1.86±0.73	0.42±0.17	2.04±0.73	0.24±0.15	0.3	1.5	8.0	9.9	10.8	0.13	0.44	8.4

NOTE: Coordinates and photometric properties of our $z \sim 9$ and $z \sim 10$ candidates. Columns 2-3: α and δ coordinates in degrees. Column 4: total magnitude in the H_{160}-band from `SExtractor` MAG_AUTO. Column 5: absolute magnitude. Columns 6-9: IR colors from `SExtractor` MAG_ISO. Columns 10-14: S/N in each band. Column 15: effective radius r_e in arcseconds measured by `SExtractor` and corrected for PSF. Column 16: stellarity index in H_{160}-band image from `SExtractor` CLASS_STAR. Column 17: photometric redshift obtained from BPZ.

Table 3
BoRG[z9-10] $z \sim 8$ candidates

Obj ID	α(J2000) (deg)	δ(J2000) (deg)	H_{160} (AB mag)	Colors Y_{105}-J_{125}	J_{125}-H_{160}	F350LP	S/N Y_{105}	J_{125}	JH_{140}	H_{160}	r_e	Stellarity	Photo-z
0116+1425_747	19.0372	+14.4068	24.99±0.18	1.12±0.36	0.26±0.14	1.3	3.2	9.9	8.4	11.6	0.25	0.03	7.9
0853+0310_145	133.1855	+3.1467	25.26±0.14	0.68±0.15	-0.07±0.12	-1.0	8.7	14.6	16.5	12.3	0.08	0.25	7.6
1103+2913_1216	165.6693	+29.2273	26.12±0.19	0.53±0.23	-0.11±0.19	0.9	5.5	8.7	8.4	7.3	0.17	0.01	7.3
1152+3402_912	177.9077	+34.0397	25.20±0.23	0.75±0.23	0.17±0.15	1.0	5.3	9.5	11.6	10.6	0.18	0.03	7.6

NOTE: Coordinates and photometric properties of our $z \sim 8$ candidates. Columns 2-3: α and δ coordinates in degrees. Column 4: total magnitude in the H_{160}-band from `SExtractor` MAG_AUTO. Columns 5-6: IR colors from `SExtractor` MAG_ISO. Columns 7-11: S/N in each band. Column 12: effective radius r_e in arcseconds measured by `SExtractor` and corrected for PSF. Column 13: stellarity index in the H_{160}-band image from `SExtractor` CLASS_STAR. Column 14: photometric redshift obtained from BPZ.

Table 4
BoRG[z9-10] step-wise rest-frame UV LF at $z \sim 8.7$ and $z \sim 10$.

z	$M_{UV,AB}$	$\phi(10^{-6}$ Mpc^{-3}mag$^{-1})$
8.7	-22.97	$3.3^{+7.7}_{-2.7}$
	-22.17	$3.7^{+8.3}_{-3.1}$
	-21.37	$6.9^{+16.2}_{-5.6}$
	-20.57	< 110
10	-23.13	< 4.7
	-22.33	$5.4^{+7.6}_{-3.5}$
	-21.53	< 12

NOTE: Upper limits are 1σ.

Table 5
BoRG[z9-10] additional high-z candidates

Obj ID	α(J2000) (deg)	δ(J2000) (deg)	H_{160} (AB mag)	Colors				S/N				r_e	Stellarity	Photo-z
				Y_{105}-J_{125}	J_{125}-H_{160}	Y_{105}-JH_{140}	JH_{140}-H_{160}	F350LP	Y_{105}	J_{125}	JH_{140}	H_{160}			
0751+2917_1211	117.7138	+29.2929	26.97±0.35	0.53±0.20	-0.66±0.23	0.43±0.20	-0.56±0.23	-0.1	6.3	10.3	10.0	5.2	ps	0.93	7.3
1209+4543_1696	182.3859	45.7250	24.96±0.40	1.47±0.51	0.31±0.13	2.15±0.51	-0.37±0.10	0.1	2.2	10.4	16.2	15.2	0.28	0.03	8.6
0853+0310_912	133.1798	+3.1730	24.99±0.16	0.94±0.13	0.48±0.25	1.10±0.24	0.32±0.12	0.6	4.8	10.4	12.7	13.4	0.18	0.02	1.6
0925+1360_965	141.2946	+14.0056	26.23±0.28	0.71±0.35	0.13±0.25	0.90±0.34	0.06±0.24	1.1	3.6	6.3	6.9	6.1	0.10	0.01	1.1
1048+1518_1140	161.9818	+15.2961	26.40±0.20	1.04±0.63	0.68±0.29	1.52±0.60	0.20±0.21	-0.1	1.9	4.5	7.3	7.4	0.08	0.19	1.9
0119-3411_22	19.7015	-34.1830	25.06±0.15	0.84±0.31	0.38±0.17	1.10±0.28	0.12±0.13	0.4	4.0	7.5	12.7	11.8	0.14	0.04	1.5

NOTE: Coordinates and photometric properties of the additional dropout candidates that are discussed in Appendix A. Columns 2-3: α and δ coordinates in degrees. Column 4: total magnitude in the H_{160}-band from `SExtractor` MAG_AUTO. Columns 5-6: IR colors from `SExtractor` MAG_ISO. Columns 7-11: S/N in each band. Column 12: effective radius r_e in arcseconds measured by `SExtractor` and corrected for PSF. Column 13: stellarity index in the H_{160}-band image from `SExtractor` CLASS_STAR. Column 14: photometric redshift obtained from BPZ.